The Astronomical Journal, 166:4 (18pp), 2023 July https://doi.org/10.3847/1538-3881/acd2dd
© 2023. The Author(s). Published by the American Astronomical Society.
OPEN ACCESS

Magnetic Field Measurements of Low-mass Stars from High-resolution Near-infrared IGRINS Spectra

Eunkyu Han[1], Ricardo López-Valdivia[2], Gregory N. Mace[1], and Daniel T. Jaffe[1]
[1] Department of Astronomy, The University of Texas at Austin, 2515 Speedway, Stop C1400, Austin, TX 78712, USA; eunkyu.han@utexas.edu
[2] Universidad Nacional Autónoma de México, Instituto de Astronomía, AP 106, Ensenada 22800, BC, México
Received 2022 November 1; revised 2023 April 20; accepted 2023 May 3; published 2023 June 6

Abstract

We present average magnetic field measurements derived from high-resolution near-infrared IGRINS spectra of a carefully selected sample of 28 M dwarfs. All 28 have reported magnetic field strengths in the literature. The main goal of this work is to investigate the accuracy, precision, and limitations of magnetic field measurements from IGRINS spectra. This investigation is critical to validating the robustness of our methods before we apply them to over 500 IGRINS-observed M dwarfs in the next paper of the series. We used the Zeeman broadening and Zeeman intensification methods to measure average magnetic fields. Our measurements are all consistent with the previous measurements to within ±1 kG, with an average offset of −0.17 kG for the broadening method and +0.19 kG for the intensification method. We find that the detection limit of IGRINS is ∼0.9 kG with the Zeeman broadening method, in accordance with the instrumental broadening limit of the spectrograph. With the Zeeman intensification method, we are able to detect down to ∼0.7 kG with a signal-to-noise ratio of 150 or greater. We find an advantage of using the intensification method over the broadening method, which is the ability to reliably measure the magnetic field strengths of stars that are cooler than 3100 K where the spectrum becomes dominated by molecular lines. Therefore, the intensification method is crucial to study stellar magnetism of late-M and brown dwarfs.

Unified Astronomy Thesaurus concepts: M dwarf stars (982); Late-type dwarf stars (906); Stellar astronomy (1583); Low mass stars (2050)

1. Introduction

Magnetic fields are ubiquitous in stars and play an important role in stellar evolution at all stages, from formation through the end of life. During the initial stages of star formation, magnetic fields provide support against gravity and regulate the collapse of molecular clouds (e.g., Mouschovias & Spitzer 1976). In young stars, magnetic fields disrupt the disk and channel the material in the inner disk onto the stellar surface (e.g., Koenigl 1991; Shu et al. 1994). In the later stages stellar winds provide magnetic braking, which leads to angular momentum loss, resulting in the slow down of stellar rotation (e.g., Schatzman 1962).

Magnetic fields are critical to stellar evolution, stellar structure, and the habitability of exoplanets. Enhanced magnetic activity can suppress convection, hindering the energy transport in the stellar interior (e.g., Chabrier et al. 2007; Morales et al. 2010; Feiden & Chaboyer 2013; MacDonald & Mullan 2013). The habitability of exoplanets is impacted by star–planet interactions because a large fraction of planetary atmospheres can be stripped away by stellar winds, detrimentally affecting the planetary environment (Barnes et al. 2011).

M dwarfs are low-mass, low-temperature main-sequence stars, with masses ranging from 0.6 $M_{\odot}$ down to the hydrogen-burning limit of 0.08 $M_{\odot}$, and they have effective temperatures ($T_{\rm eff}$) ranging from 3800 to 2300 K. M dwarfs outnumber all other spectral types in the solar neighborhood, making up over 70% of the population by number (e.g., Chabrier 2003; Bochanski et al. 2010; Henry et al. 2018; Winters et al. 2019). M dwarfs are also known as exoplanet hosts (e.g., Dressing & Charbonneau 2013; Gaidos et al. 2014; Hardegree-Ullman et al. 2019). Therefore, to study the habitability of exoplanets a detailed characterization of their magnetism is required.

Observations show the active nature of M dwarfs including: Hα or Ca II emission from the chromosphere (e.g., Wilson 1966; Noyes et al. 1984; Soderblom et al. 1993), X-ray coronal emission (e.g., Pallavicini et al. 1981; Pizzolato et al. 2003), radio emission from accelerated electrons (e.g., Stewart et al. 1988; Berger 2006), spots, and flares, all of which indicate the presence of magnetic fields (e.g., Donati et al. 2008; Browning et al. 2010; Hawley et al. 2014; Astudillo-Defru et al. 2017). In particular, studies show that the measured magnetic field strengths of these stars are several kG (e.g., Johns-Krull & Valenti 1996; Reiners & Basri 2007, 2009, 2010). However, the formation mechanism of magnetic fields within M dwarfs is not understood. For Sun-like stars, the $\alpha\Omega$ dynamo is thought to generate large-scale magnetic fields (e.g., Parker 1955; Moffatt 1978; Stix 1981; Ossendrijver 2003; Charbonneau 2014), where differential rotation stretches the star's poloidal field and creates a toroidal field (the Ω effect). Then, the interaction between convection and rotation regenerates a poloidal field from a toroidal field (the α effect). The Ω effect is believed to occur at the tachocline (e.g., Parker 1975; Dikpati & Charbonneau 1999), which is the boundary between the convective and radiative layers. Partially convective M dwarfs ($0.35M_{\odot} < M_{*} < 0.6M_{\odot}$) have tachoclines and are believed to follow the solar $\alpha\Omega$ dynamo. However, fully convective M dwarfs ($0.1M_{\odot} < M_{*} < 0.35M_{\odot}$) lack the tachocline (Chabrier & Baraffe 1997), and therefore, the $\alpha\Omega$ dynamo cannot operate to produce magnetic fields. As an alternative, a turbulent dynamo was proposed by Durney et al. (1993). In this scenario, a turbulent convective velocity generates small-scale chaotic

Original content from this work may be used under the terms of the Creative Commons Attribution 4.0 licence. Any further distribution of this work must maintain attribution to the author(s) and the title of the work, journal citation and DOI.

magnetic fields. However, these small-scale magnetic fields cannot support the high levels of activities observed with the fully convective M dwarfs. A more recent study by Chabrier & Küker (2006) showed that an α^2 dynamo is capable of generating a large-scale magnetic field in fully convective M dwarfs, but the dependence on stellar rotation has not been settled (e.g., Favier & Bushby 2013).

Empirical determinations of the magnetic field strengths of M dwarfs are critical to testing the theoretical models of stellar interiors and the habitability of exoplanets found to orbit these stars. There are two direct ways to measure the surface magnetic fields of M dwarfs and one indirect way to map the structure of the fields, all of which involve the Zeeman effect (Zeeman 1897). The Zeeman effect involves the splitting of spectral lines in the presence of an external magnetic field, where the energy level of an atomic transition is split into three sublevels, resulting in the emergence of an unperturbed π component and red- and blueshifted σ components. The energy shifts between the σ and the π components are given by

$$\Delta E = g\frac{e\hbar}{2m_e c}BM, \quad (1)$$

where g is the Landé factor, B is the strength of the magnetic field, and M is the magnetic quantum number. The first direct method to determine the magnetic field strength is to measure Zeeman broadening in spectral lines (e.g., Saar 1988; Landstreet 1992), the second direct method is to measure Zeeman intensification in spectral lines (Basri et al. 1992; Basri & Marcy 1994), and the indirect method is to measure Doppler shifts in polarized spectra using the Zeeman Doppler Imaging (ZDI; e.g., Donati et al. 1989; Semel 1989; Brown et al. 1991; Semel et al. 1993; Donati & Brown 1997). These methods complement each other; while the first and the second methods provide an integrated magnetic field strength over the stellar surface, the last method provides information about the topology of the fields.

Since the first direct measurement of the photospheric magnetic field of an M dwarf (Saar & Linsky 1985), several efforts have been made to empirically determine M dwarf magnetic field strengths. One challenge has been the limited number of atomic lines that distinguish between the effects of the magnetic field and other stellar parameters. The other challenge is fast stellar rotation where line shapes and profiles get blurred out by rotational broadening. A recent study (Hussaini et al. 2020) found that the minimum measurable magnetic field strength using Zeeman broadening of $R = 45{,}000$ Immersion GRating INfrared Spectrometer (IGRINS, Yuk et al. 2010) spectra is primarily limited by the projected rotational velocity ($v\sin i$). When using the Ti region around 2.22 μm, magnetic field strengths in kG lower than one-tenth of the value of $v\sin i$ in km s^{-1}are not detectable. For instance, for a star with $v\sin i$ of 20 km s^{-1}, the Zeeman broadening method using the Ti I line around 2.22 μm can only reliably measure a magnetic field strength of 2.0 kG or greater.

To date, about 300 M dwarfs have empirically determined magnetic field strengths (see Figure 1), and only a handful of them have multiple measurements. High-resolution near-infrared spectroscopy is pivotal to directly measuring M dwarf magnetic field strengths. M dwarfs are brightest in the near-infrared and the magnitude of the Zeeman effect has a λ^2-dependence, enabling the measurement of lower magnetic fields in the infrared than at optical wavelengths. IGRINS, a high-resolution near-infrared spectrograph, has observed hundreds of M dwarfs since its commissioning in 2014 (e.g., Mann et al. 2016; Han et al. 2017, 2019; Kesseli et al. 2018; Sawczynec et al. 2022) providing an unprecedented data set to investigate magnetism of M dwarfs.

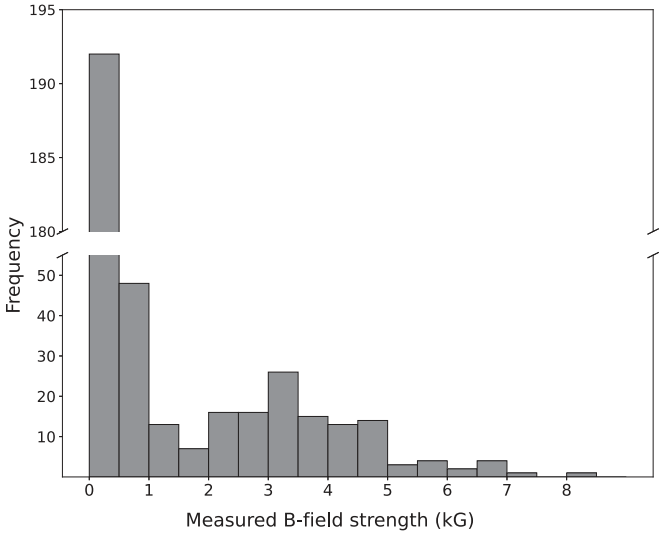

Figure 1. Compiled magnetic field strength measurements of M dwarfs using Zeeman broadening and intensification from literature. See Kochukhov (2021) and Reiners et al. (2022) for the references.

In this paper, we present magnetic field measurements of a carefully selected sample of 28 M dwarfs (see Table 1 for the list) observed with IGRINS, all of which have reported magnetic field strengths from the literature. This set of M dwarfs tests whether the magnetic field strengths measured with IGRINS are consistent with the literature. This comparison provides a "proof of principle" for future magnetic field determinations using the larger IGRINS sample.

2. Data and Observations

2.1. IGRINS Observations

IGRINS is a cross-dispersed, high-resolution ($R = \lambda/\Delta\lambda = 45{,}000$) near-infrared (1.45–2.5 μm) spectrograph that obtains simultaneous observations of both H and K band in a single exposure (Yuk et al. 2010; Park et al. 2014; Mace et al. 2016, 2018). IGRINS has traveled to three different telescopes: the 2.7 m Harlan J. Smith Telescope at the McDonald Observatory in Texas, the 4.3 m Lowell Discovery Telescope (LDT, formerly known as Discovery Channel Telescope) in Arizona, and the 8.1 m Gemini South telescope in Chile. Because there are no moving parts in the optics systems, all data products have a fixed spectral format and stability regardless of the telescope. All IGRINS spectra used in this work were taken during its visits to the McDonald and the Lowell observatories, between 2014 and 2019.

We observed the science targets, followed by observations of A0V standard stars within 0.1 airmasses for telluric corrections. For all our observations we performed ABBA slit nodding. On each night, we took dark, flat fields, and an empty sky frame for calibration purposes. To reduce the spectra, we used a publicly available reduction pipeline for IGRINS (Lee et al. 2017).[3] The

[3] https://github.com/igrins/plp/tree/v2.1-alpha.3

Table 1
Selected Parameters for the 28 M Dwarfs in this Study

Target	SpT	*T*eff (K)	*B* (kG)	References	Target	SpT	*T*eff (K)	*B* (kG)	References
GJ 51	M5.0	3200	6.1 ± 0.2	9	GJ 406	M5.5	2800	2.3 ± 0.3	5
			4.8 ± 0.3	10				2.3 ± 0.3	7
Barta 161 12	M4.0	3400	5.8 ± 1.0	10	GJ 412B	M6.0		7.3 ± 0.3	9
G 80-21	M3.0	3500	3.2 ± 0.1	10	GJ 1156	M5.0	3200	3.6 ± 0.7	9
		3473	3.49 ± 0.2	11			3064	3.97 ± 0.46	11
GJ 182	M0.0		2.6 ± 0.6	9	GJ 569A	M2.0		1.8 ± 0.1	9
GJ 3322	M4.0		2.75	6	GJ 3877	M7.0	2600	2.2 ± 0.2	5
GJ 208	M0.0	3800	1.2 ± 0.3	10	GJ 644 C	M3.5	2600	2.8 ± 0.1	5
		4067	1.10 ± 0.06	11				2.8 ± 0.4	10
GJ 3379	M4.0	3400	2.5 ± 1.0	10			3005	3.02 ± 0.20	11
		3296	2.49 ± 0.22	11	V1274 Her	M5.5	3000	6.9 ± 1.0	10
GJ 285	M4.5	3300	3.3	3	G 227-22	M5.0	3400	4.3 ± 0.9	10
			4.5	4	GJ 4053	M4.5	3300	2.0 ± 1.6	10
			4.5 ± 0.2	5	GJ 1227	M4.0	3294	0.50 ± 0.22	11
			3.6 ± 0.1	7	GJ 752B	M8.0	2500	2.3 ± 0.2	10
			4.8 ± 0.2	9			2500	1.21 ± 0.18	11
			4.6 ± 0.3	10	GJ 1243	M4.0	3400	3.2 ± 1.0	10
		3251	4.54 ± 0.15	11	GJ 803	M1.0		2.3	2
GJ 299	M4.5	3245	0.92 ± 0.09	11			3700	3.01 ± 0.22	11
GJ 1111	M6.5	2700	3.2 ± 0.5	9	GJ 873	M4.0	3400	3.7	2
			3.3 ± 0.6	10				3.9	3
GJ 388	M3.5		2.8 ± 0.3	1				3.7 ± 0.2	5
			2.6	2				3.8 ± 0.5	8
			3.3	3				4.2 ± 0.3	9
			3.2	4				4.1 ± 0.2	10
			3.3 ± 0.1	5			3306	4.32 ± 0.11	11
			2.9 ± 0.2	7	GJ 9799	M3.0	3500	3.4 ± 0.6	10
			3.1 ± 0.2	9			3335	3.87 ± 0.34	11
GJ 3622	M6.5		1.4 ± 0.2	9	GJ 896A	M3.5		3.6 ± 0.3	9
					GJ 896B	M4.5		4.2 ± 1.0	9

References. (1) Saar & Linsky (1985); (2) Saar (1994); (3) Johns-Krull & Valenti (2000); (4) Kochukhov et al. (2009); (5) Afram et al. (2009); (6) Shulyak et al. (2011); (7) Shulyak et al. (2014); (8) Kochukhov & Lavail (2017); (9) Shulyak et al. (2017); (10) Shulyak et al. (2019); (11) Reiners et al. (2022).

pipeline processes flat fields, calculates the wavelength solution from the sky frame, performs AB subtraction to remove the OH airglow emission lines, and optimally extracts the spectrum. The pipeline then divides the target spectrum by a Vega-corrected A0V telluric standard. For objects with multi-epoch observations, we coadded the spectra to produce a single higher signal-to-noise ratio (S/N) spectrum.

2.2. iSHELL Observations

iSHELL is a cross-dispersed near-infrared spectrograph (Rayner et al. 2022) on NASA's InfraRed Telescope Facility (IRTF). Like IGRINS, iSHELL employs a silicon immersion grating as the primary disperser (Marsh et al. 2007; Gully-Santiago et al. 2014). It provides 19 modes that cover segments of wavelength from ~1.1 to 5.3 μm, and two slit options that give resolving powers of $R = \lambda/\Delta\lambda = 35{,}000$ and $R = \lambda/\Delta\lambda = 75{,}000$. To understand the effect of spectral resolution on the sensitivity and accuracy of magnetic field detection using the IGRINS spectra, we observed all targets in our sample with iSHELL using the $0\farcs375$ slit, resulting in a higher resolution of $R = \lambda/\Delta\lambda = 75{,}000$. In addition, to match IGRINS *K*-band coverage, we used the K2 filter, resulting in a wavelength coverage from 2.09 to 2.38 μm. All observations were made on nights in 2021 August, October, November, and December, and 2022 February.

For all iSHELL observations, we carefully planned to match the highest S/N of each target's IGRINS spectra whenever possible. The exposure times were calculated based on the online iSHELL Exposure Time Calculator[4] and were modified as needed during the observations. We observed science targets, each of which was followed by calibration observations including dome flats and arc lamps at the target position. We also observed A0V telluric standards but these observations were shared between science targets if the differences in position and airmass were within 10° and $0\fdg1$, respectively. For reduction, we used iSHELL version of `Spextool` (Cushing et al. 2004) and corrected for the telluric using `xtellcor` (Vacca et al. 2003). We removed bad pixels by masking and then interpolating across them.

3. Stellar Parameter Determinations

Precise magnetic field measurements require knowledge of $T_{\rm eff}$, $v\sin i$, and surface gravity ($\log g$) for each star. Although most of the M dwarfs in our sample have reported $T_{\rm eff}$, $v\sin i$, and $\log g$ values from the literature, some stars were missing those parameters. To maintain consistency in the measurements, we determined $T_{\rm eff}$ and $v\sin i$ ourselves. For $\log g$, we adopted $\log g = 5.0$ dex throughout the analysis, which is the middle value of the typical $\log g$ ranges (4.5–5.5 dex) of low-mass stars. The reported $\log g$ values of the stars in our sample range from 4.7 to 5.3 dex.

[4] http://irtfweb.ifa.hawaii.edu/ishell/iSHELL_Exposure_Time_Calculator/.

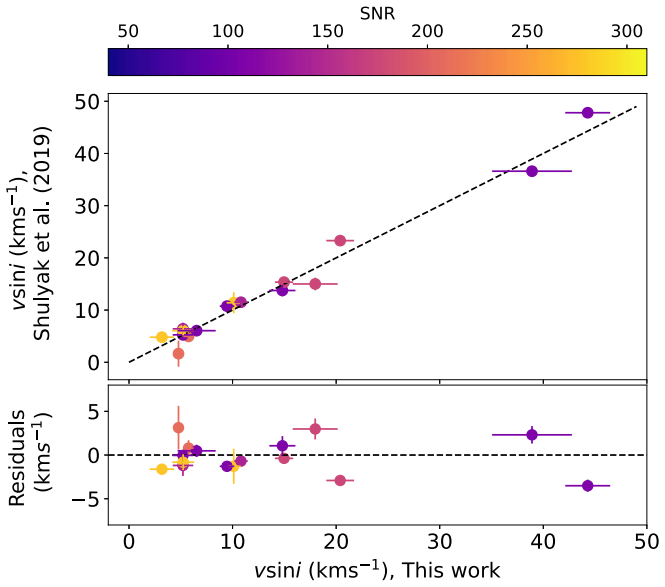

Figure 2. Comparison of *v*sin*i* measurements from this work to values from Shulyak et al. (2019). The bottom panel shows the difference between Shulyak et al. (2019) and this work.

To calculate $T_{\rm eff}$ for the objects in our sample, we used the color–$T_{\rm eff}$ relation from Mann et al. (2015). For the targets with *V*- and *J*-band magnitudes available, we used $V-J$ and $J-H$ colors. For these objects without *V*-band magnitudes in the literature, we used the Gaia $G_{\rm BP}$ and $G_{\rm RP}$ magnitudes together with the $J-H$ colors. The color–$T_{\rm eff}$ relations from Mann et al. (2015) result in $T_{\rm eff}$ values consistent with the reported values from the literature for most of the targets. However, GJ 208, GJ 3379, GJ 285, GJ 1156, GJ 1243, and GJ 4053 differ by 100–200 K. GJ 644 C differed by 100–300 K, and GJ 752B differed by 700 K. In these cases, we measured magnetic fields using both the literature $T_{\rm eff}$ and the $T_{\rm eff}$ calculated using the color–$T_{\rm eff}$ relation from Mann et al. (2015).

To calculate *v*sin*i*, we used a cross-correlation method to measure the rotational broadening of each star (e.g., Delfosse et al. 1998; Mohanty & Basri 2003; West & Basri 2009; Muirhead et al. 2013; Kesseli et al. 2018). We cross-correlated the target spectrum with a slow rotator spectrum and converted the width of the cross-correlation function to the *v*sin*i*. For IGRINS spectra we used HD 173739, a known slow rotator with $v\sin i = 3.29 \pm 0.09$ km s^{-1} (Moutou et al. 2020) and for the iSHELL spectra we used GJ 3379 with $v\sin i = 5.6 \pm 0.1$ km s^{-1} (Shulyak et al. 2019), which is the slowest rotator spectrum we had since there were no iSHELL spectra of HD 173739 available for the *K* band. For the *v*sin*i* measurements, and to maintain consistency between the IGRINS and the iSHELL spectral analysis, we only used the IGRINS *K*-band spectra. We carefully examined the entire IGRINS *K*-band spectral region and removed any order that is dominated by telluric lines. We also excluded the order that contains the Na doublet near 2.2 μm since the inclusion of that line can lead to inaccurate *v*sin*i* measurement due to pressure broadening. These vetting processes left us with a total of nine orders in the *K* band, covering from 2.057 to 2.186 μm and from 2.209 to 2.386 μm. These regions include the CO bands beyond $\sim$2.3 μm, which play an important role in determining *v*sin*i*.

We compared our *v*sin*i* measurements with those from Shulyak et al. (2019; see Figure 2). Shulyak et al. (2019) measured *v*sin*i* of M dwarfs from the CARMENES spectra using two sets of lines: the Ti lines at 960–980 nm and the FeH lines at 990–995 nm. They adopt magnetic field measurements from the average of the two sets of lines if a star has $v\sin i < 20$ km s^{-1}. For stars with $v\sin i > 20$ km s^{-1}, they report the measurements from the Ti lines only. This methodological difference is due to the blending of the FeH lines with nearby lines when the *v*sin*i* is large. Therefore, for the *v*sin*i* comparisons, we took their average *v*sin*i* values for stars with $<$20 km s^{-1} and Ti *v*sin*i* values for stars with $>$20 km s^{-1}. The top panel in Figure 2 shows *v*sin*i* from Shulyak et al. (2019) versus those from this work, colored by the S/N of the IGRINS spectra. The bottom panel shows the difference between our measurements and those from Shulyak et al. (2019). We find that our measurements generally agree to within 2 km s^{-1} with those from Shulyak et al. (2019) for stars with *v*sin*i* $<$20 km s^{-1}. Note the relatively large errors for the two stars with the largest *v*sin*i*, which are due to the low S/N of the IGRINS spectra. Kesseli et al. (2018) also found that a spectrum with S/N lower than 100 yields large uncertainties. Table 3 shows the *v*sin*i* measurements from this work. The typical dispersion of our *v*sin*i* measurements is in good agreement with those of Kesseli et al. (2018) who used the same cross-correlation method to measure the *v*sin*i*s. Our dispersion is a factor of 2 smaller than those of López-Valdivia et al. (2023) who determined *v*sin*i* along with $T_{\rm eff}$, $\log g$, and magnetic field strength through a Markov chain Monte Carlo (MCMC) analysis.

4. Magnetic Field Measurements

To measure the average magnetic field strengths of M dwarfs in our sample, we used the two direct methods that were briefly mentioned in Section 1, both of which are based on measuring the Zeeman effects in the stellar spectrum. One is to measure Zeeman broadening of the spectral lines, and the other is to measure Zeeman intensification.

We used the Vienna Atomic Line Database (VALD3 Ryabchikova et al. 2015) to obtain information on atomic transitions. Both Zeeman broadening and intensification measurements allow the averaged measurements of magnetic field strength across the stellar surface. In the following subsections, we discuss each method in detail. All data processing and analysis of the IGRINS and iSHELL spectra were performed in the same way to maintain consistency.

4.1. Zeeman Broadening of Spectral Lines

The basis of measuring Zeeman broadening lies in detecting the excess in the broadening of spectral lines with high Landé values in comparison to those lines with lower Landé values. The magnitude of the effect in a stellar spectrum can be calculated by

$$\Delta\lambda = 4.67 \times 10^{-6} g_{\rm eff} \lambda_0^2 B \quad (2)$$

$$\Delta v_B = 1.4 g_{\rm eff} \lambda_0 B, \quad (3)$$

where $\Delta\lambda$ and Δv_B are the magnitudes of Zeeman broadening in μm and km s^{-1}, respectively, $g_{\rm eff}$ is the effective Landé factor, λ_0 is the central position of the unsplit line in μm, and B is the magnetic field strength in kG. The λ_0^2-dependence on the broadening makes the near-infrared regime favorable for

investigation. The $g_{\rm eff}$ value represents how sensitive a spectral line is to the magnetic fields.

There are two important conditions to see the magnetic split in the spectral lines. One is to have a strong enough magnetic field that produces detectable wavelength separation and the other is to have high-resolution spectra to resolve the split. If these conditions are not met, the lines will appear as broadened and become hard to distinguish from the rotational broadening. Furthermore, because the convective dynamos are driven by stellar rotation, stellar rotation is correlated with stellar magnetism, producing a strong magnetic field when rotating fast (e.g., Pallavicini et al. 1981; Pizzolato et al. 2003). Therefore, there is a trade-off between high $v\sin i$ and the detectability of the line broadening. Thanks to the wide wavelength coverage of IGRINS, we have access to an ample number of lines that allow us to distinguish magnetic broadening from rotational broadening.

In the absence of a magnetic field, the line width is dominated by other broadening mechanisms such as instrumental, rotational, and microturbulent broadening. For low-mass stars, typical values of microturbulence are 1–2 km s^{-1}, which is much less than the pressure or thermal broadening (Reid & Hawley 2005). Given the resolving powers of IGRINS and iSHELL, the instrumental broadening is $\sim$7 km s^{-1} and $\sim$4 km s^{-1}, respectively. In practice, to reliably detect the magnetic field strength, Zeeman broadening should result in Δv_B of at least equal to or greater than the sum of the instrumental and rotational broadening. If looking at a magnetically sensitive line such as Ti at 2.23 μm, Equation (3) translates to $\Delta v_B = 8.05$ km s^{-1} kG^{-1}. For a line whose line width is dominated by Zeeman broadening, we can detect a magnetic field as weak as $\sim$0.9 kG with IGRINS and $\sim$0.5 kG with iSHELL. Therefore, it is important to choose atomic lines with high $g_{\rm eff}$ values to maximize the detectability. Table 2 contains the information on atomic lines that were used in this work.

To measure Zeeman broadening, we first processed all of the pipeline-reduced spectra further by stitching the individual orders together and fitting the continuum for each *H*- and *K*-band spectrum. Unlike F, G, and K dwarfs, finding the continuum of M dwarfs is challenging due to the presence of molecular lines across all wavelength ranges (e.g., Tsuji & Nakajima 2014). Therefore, instead of fitting a continuum for entire spectral regions, we fit for a local pseudocontinuum using small regions around individual atomic lines. When the spectrum is stitched and normalized, we shifted the spectrum to 0 km s^{-1} radial velocity space to match the central locations of each line to the positions given in Table 2. We then fit a double-Lorentzian function to each line, as was identified by Hussaini et al. (2020) as providing a good match to IGRINS spectra. For the fitting procedure, we set the amplitude and the FWHM of each component Lorentzian in the double-Lorentzian function to be the same while varying the central positions. We employed the Levenberg–Marquardt technique and performed χ^2 minimization through `mpfit` to find the best-fit double-Lorentzian function (Markwardt 2009). However, if the star's $v\sin i$ was greater than 15 km s^{-1}, we switched the double-Lorentzian to a double-Gaussian function. This procedural change avoids overestimation of the separation in the process of reducing the chi-square and properly captures the parabolic shape of the lines from the rotational broadening. We took the shift in λ obtained from the fitting and converted it to magnetic field strength using Equation (2). Figure 3 shows the fitting results for GJ 388 where the top panel shows the IGRINS *K*-band region of interest with each atomic line marked at its position. The smaller bottom panels are the zoom-in view of individual lines with each line name and its $g_{\rm eff}$ value marked. Solid red lines are the best-fit double-Lorentzian and the dashed red lines are the component single-Lorentizans. We removed any line measurement with chi-squared greater than 3σ from the mean or below the instrumental broadening (0.9 ± 0.5 kG), and those panels are grayed out in Figure 3. We report the average and the standard deviation of all valid measurements as final values in Table 3.

4.2. Zeeman Intensification of Spectral Lines

Perturbation of atomic transitions due to the presence of magnetic fields often leads to the desaturation of strong absorption lines, a phenomenon known as Zeeman intensification. The splitting of an atomic line into its Zeeman components affects the optical depth of the line center and the wings; the optical depths decrease at the center while they increase at the wings. These processes result in reduced saturation at the line center and an enhancement of the equivalent width (EW) of the spectral line. The first practical application was by Basri et al. (1992) who used it for a solar-type star, followed by several groups since then (e.g., Basri et al. 1992; Kochukhov et al. 2020; Muirhead et al. 2020). Zeeman intensification increases as a function of magnetic field strength until all the Zeeman components of a line are fully resolved. However, unlike in the case of Zeeman broadening of spectral lines where higher $g_{\rm eff}$ values correspond to broader lines, the enhancement of EWs from Zeeman intensification is more prominent for the spectral lines with a large number of widely separated Zeeman components and not necessarily for the lines with high $g_{\rm eff}$ values. The enhancement also depends on the opacity, where an optically thin line would show no EW enhancement. Unlike Zeeman broadening, the degree of Zeeman intensification cannot be expressed analytically. It is an outcome of the complex interplay of the number of Zeeman components, the line strength and the opacity, as well as the variation of the line and continuum source functions along with line depth.

The Zeeman intensification method has two major advantages over the Zeeman broadening method. First, it is less demanding of high S/N because the method relies on the EW of the lines and not on the detailed line profiles. More importantly, the Zeeman intensification method is not affected by $v\sin i$, allowing for magnetic field measurements of rapid rotators. However, challenges also exist for the Zeeman intensification method since it is model dependent. The method heavily relies on the accuracy of atomic parameters, in particular, the transition probabilities ($\log gf$). In addition, a radiative transfer code incorporating polarization from magnetic fields is required to model the Zeeman intensification of spectral lines. To distinguish the enhancement of EWs arising from the magnetic field rather than other stellar parameters, multiple lines must be compared, which generally requires a wide range of wavelength coverage in the observations.

To measure the magnetic field strengths using the Zeeman intensification method, we first generated model spectra using the MOOGStokes code (Deen 2013). MOOGStokes is a customized version of the MOOG code (Sneden 1973), which is a one-dimensional Local Thermodynamical Equilibrium (LTE) radiative transfer code. MOOGStokes incorporates

Table 2
Details of the Atomic Line Information

Line	Wavelength (Å)	log *gf*	$g_{\rm eff}$	Lower State	Upper State	Group
Fe I	15294.5603	0.719	1.590	3d6.(5D).4s (6D).5 s e7D	3d6.(5D).4s (6D).5p n7D*	1
Fe I	15621.6542	0.589	1.494	3d6.(5D).4s (6D).5 s e5D	3d6.(5D).4s (6D).5p t5D*	1
Fe I	15769.4226	0.700	1.202	3d6.(5D).4s (6D).5 s e5D	3d6.(5D).4s (6D).5p u5F*	1
Fe I	15818.1422*	0.589	1.131	3d6.(5D).4s (6D).5 s e5D	3d6.(5D).4s (6D).5p u5F*	1
Fe I	16102.408	0.546	1.163	3d7.(4F).5 s e5F	3d7.(4F).5p 5G*	2
Fe I	16486.6664*	0.783	1.117	3d7.(4F).5 s e5F	3d7.(4F).5p 5G*	2
Fe I	16444.8156	0.663	1.405	3d7.(4F).5 s e5F	3d7.(4F).5p 5F*	2
Ti I	15186.7114	−2.385	1.510	3d3.(2G).4 s a3G	3d2.(3F).4 s.4p.(3P*) z3G*	3
Ti I	15334.8465	−1.010	1.210	3d3.(2G).4 s a3G	3d2.(3F).4 s.4p.(3P*) z3G*	3
Ti I	15543.7583	−1.134	1.055	3d3.(2G).4 s a3G	3d2.(3F).4 s.4p.(3P*) z3G*	3
Ti I	15698.9763	−2.105	1.530	3d3.(2G).4 s a3G	3d2.(3F).4 s.4p.(3P*) z3G*	3
Ti I	15715.5727*	−1.224	0.745	3d3.(2G).4 s a3G	3d2.(3F).4 s.4p.(3P*) z3G*	3
Ti I	15836.7902	−2.165	1.525	3d3.(2G).4 s a3G	3d2.(3F).4 s.4p.(3P*) z3G*	3
Ca I	16136.8231*	−0.363	0.499	3p6.4 s.5p 3P*	3p6.4 s.5d 3D	4
Ca I	16150.7624	−0.032	1.002	3p6.4 s.5p 3P*	3p6.4 s.5d 3D	4
Ca I	16155.2357	−0.496	0.997	3p6.4 s.5p 3P*	3p6.4 s.5d 3D	4
Ca I	16197.0748	0.254	1.167	3p6.4 s.5p 3P*	3p6.4 s.5d 3D	4
Ca I	16204.087	−0.497	1.334	3p6.4 s.5p 3P*	3p6.4 s.5d 3D	4
Mg I	15740.706*	−0.212	99.00	3 s.4p 3P*	3 s.4d 3D	5
Mg I	15748.988	0.140	99.00	3 s.4p 3P*	3 s.4d 3D	5
Mg I	15765.839	0.411	99.00	3 s.4p 3P*	3 s.4d 3D	5
Ca I	19309.2217	−1.000	0.502	3p6.4 s.4p 3P*	3p6.3d.4 s 3D	6
Ca I	19452.9815*	−0.651	0.993	3p6.4 s.4p 3P*	3p6.3d.4 s 3D	6
Ca I	19505.7388	−1.129	1.002	3p6.4 s.4p 3P*	3p6.3d.4 s 3D	6
Ca I	19776.7712	−0.388	1.155	3p6.4 s.4p 3P*	3p6.3d.4 s 3D	6
Ca I	19862.1915	−1.138	1.332	3p6.4 s.4p 3P*	3p6.3d.4 s 3D	6
Ca I	19917.1948	−2.315	2.000	3p6.4 s.4p 3P*	3p6.3d.4 s 3D	6
Ca I	19853.0919*	0.399	1.251	3p6.4 s.5 s 3S	3p6.4 s.5p 3P*	7
Ca I	19933.7274	0.171	1.749	3p6.4 s.5 s 3S	3p6.4 s.5p 3P*	7
Ca I	19961.8318	−0.302	2.002	3p6.4 s.5 s 3S	3p6.4 s.5p 3P*	7
Ca I	20962.4100	−0.703	1.167	3p6.4 s.4d 3D	3p6.4 s.6p 3P*	8
Ca I	20972.5288	−0.977	1.000	3p6.4 s.4d 3D	3p6.4 s.6p 3P*	8
Ca I	20973.3779*	−1.331	0.499	3p6.4 s.4d 3D	3p6.4 s.6p 3P*	8
Ca I	22607.9445	0.516	0.749	3p6.4 s.4d 3D	3p6.4 s.4f 3F*	9
Ca I	22624.9618	0.687	1.001	3p6.4 s.4d 3D	3p6.4 s.4f 3F*	9
Ca I	22626.7233*	−0.216	0.917	3p6.4 s.4d 3D	3p6.4 s.4f 3F*	9
Ca I	22651.1773	0.847	1.126	3p6.4 s.4d 3D	3p6.4 s.4f 3F*	9
Ca I	22653.5794	−0.216	1.209	3p6.4 s.4d 3D	3p6.4 s.4f 3F*	9
Ti I	21782.9203*	−1.109	1.285	3d3.(4P).4 s a5P	3d2.(3F).4 s.4p.(3P*) z5D*	10
Ti I	21897.3764	−1.398	1.160	3d3.(4P).4 s a5P	3d2.(3F).4 s.4p.(3P*) z5D*	10
Ti I	22211.2179	−1.718	2.075	3d3.(4P).4 s a5P	3d2.(3F).4 s.4p.(3P*) z5D*	10
Ti I	22232.8431	−1.606	1.660	3d3.(4P).4 s a5P	3d2.(3F).4 s.4p.(3P*) z5D*	10
Ti I	22274.0067	−1.705	1.575	3d3.(4P).4 s a5P	3d2.(3F).4 s.4p.(3P*) z5D*	10
Na I	22056.426	0.290	99.00	2p6.4 s 2S	2p6.4p 2P*	11
Na I	22083.662	−0.020	99.00	2p6.4 s 2S	2p6.4p 2P*	11

Note. The line information was obtained from the VALD3 database (Ryabchikova et al. 2015) at http://vald.astro.uu.se/vald/php/vald.php. For the *H*-band Mg I and the *K*-band Na I lines, the $g_{\rm eff}$s were missing and returned as 99.00. * denotes the spectral line that is assigned as the denominator in the EW ratio determination.

Stokes polarization vectors into MOOG and calculates the disk-averaged emergent spectrum in the presence of stellar magnetic fields. The field geometry is assumed to be uniform and radial. This is a much simpler form than the magnetic field geometry in real stars, but it is the simplest form known to be consistent with observations (e.g., Valenti et al. 1995). MOOSGTOKES takes the one-dimensional MARCS atmospheric model (Gustafsson et al. 2008),[5] the line list from VALD along with user-input parameters (magnetic field strength, *v*sin*i*, and the spectral resolution) to synthesize a model spectrum. Since our main interest lies in the magnetic field measurements, we used a fixed set of values for the metallicity, microturbulence, and log *g* when selecting MARCS models. Most objects have reported metallicity ranging from −0.5 to 0.48 dex (e.g., Neves et al. 2013; Dittmann et al. 2016; Gáspár et al. 2016) and the ones without reported metallicity have low radial velocities that are less than 30 km s^{-1}, which are likely to be disk population. For low-mass stars, typical values of the microturbulence are 1–2 km s^{-1}, which is much less than the pressure or thermal broadening (Reid & Hawley 2005) and log *g* ranges from 4.5 to 5.5 dex. For this analysis, we chose solar metallicity, microturbulence of 1 km s^{-1}, and log *g* of 5 dex.

For the MOOGStokes model synthesis, we used a grid of stellar parameters spanning $T_{\rm eff}$ from 2500 to 4000 K with a

[5] https://marcs.astro.uu.se/

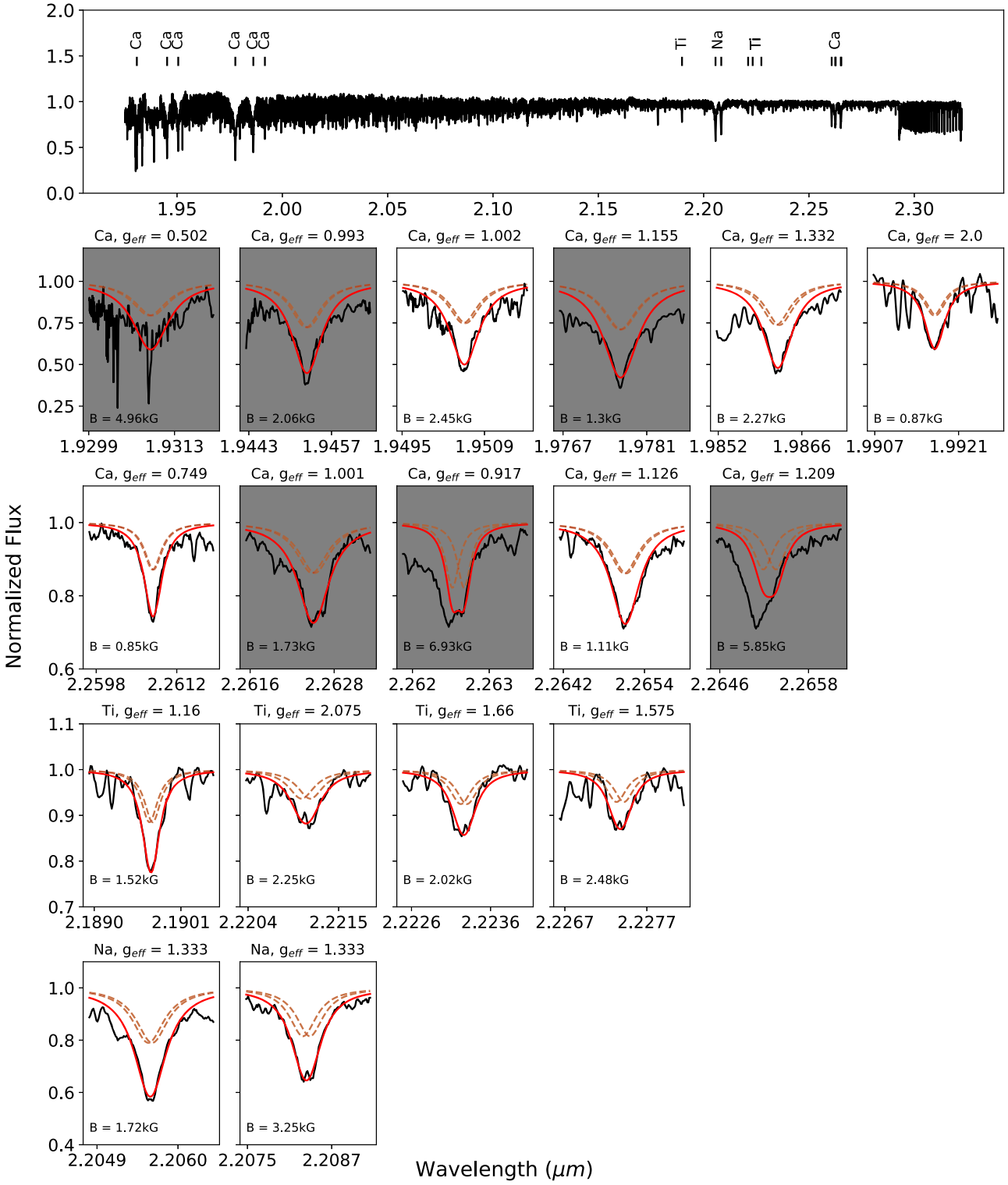

Figure 3. Sample Zeeman broadening measurements of GJ 388. The top panel shows the IGRINS *K*-band region of interest with each atomic line position marked. The smaller bottom panels are the zoom-in view of individual lines with each line and its $g_{\rm eff}$ value marked. Solid red lines are the best-fit double-Lorentzian and the dashed red lines are the component single-Lorentizans. The grayed panels are excluded from the final statistics due to being a bad measurement or below the detection limit. The weighted average and uncertainty for this target are 2.64 ± 0.59 kG.

step of 100 K, magnetic field strengths from 0 to 8.5 kG with a step of 0.5 kG, and *v*sin*i* from 0 to 50 km s^{-1} with a step of 1 km s^{-1}. For the magnetic field strength and the *v*sin*i*, the ranges were chosen to ensure the full coverage of stellar parameters from the literature. The $T_{\rm eff}$ range was chosen to cover the effective temperatures of M dwarfs, but the coolest MARCS models available are 2500 K.

Figure 4 shows three sample MOOGStokes models of $T_{\rm eff} = 3300$ K and *v*sin*i* $= 0$ km s^{-1} with different magnetic field strengths (0.5, 2.5, and 4.5 kG) that were used in building

Table 3
Measured Stellar Parameters

Target	$v\sin i$ (km s^{-1})	$v\sin i_{\rm err}$ (km s^{-1})	$T_{\rm eff}$ (K)	Instrument	Zeeman Intensification		Zeeman Broadening		S/N
					B (kG)	$B_{\rm err}$ (kG)	B (kG)	$B_{\rm err}$ (kG)	
GJ 51	10.81	0.65	3180	IGRINS	4.61	0.50	4.16	0.33	136
GJ 51	10.90	1.55	3180	iSHELL	4.64	0.28	5.63	0.66	210
GJ 3379	5.23	1.06	3238	IGRINS	2.31	0.54	2.20	0.60	513
GJ 3379	5.31	0.78	3238	iSHELL	2.16	0.50	2.34	0.04	240
GJ 285	5.75	0.50	3152	IGRINS	4.87	0.48	4.55	0.35	222
GJ 285	6.24	0.58	3152	iSHELL	4.97	0.30	6.05	0.52	120
GJ 299	6.80	0.40	3169	IGRINS	1.60	0.50	0.90	0.50	153
GJ 299	4.34	0.88	3169	iSHELL	1.27	0.33	0.90	0.29	100
GJ 1111	10.34	0.59	2836	IGRINS	3.34	0.54	3.22	0.11	250
GJ 1111	9.29	0.44	2836	iSHELL	4.01	0.34	3.32	0.34	250
GJ 3622	4.85	1.40	2856	IGRINS	1.20	0.60	1.13	0.12	230
GJ 3622	5.60	0.76	2856	iSHELL	1.68	0.22	…	…	110
GJ 406	4.84	0.89	2793	IGRINS	2.63	0.46	2.29	0.69	427
GJ 406	4.89	0.70	2793	iSHELL	3.50	0.19	2.76	0.13	180
GJ 412B	4.74	0.60	2857	IGRINS	5.58	0.48	5.06	0.28	139
GJ 412B	4.94	0.78	2857	iSHELL	5.01	0.40	…	…	140
GJ 1156	14.97	0.88	2994	IGRINS	3.21	0.51	3.13	0.75	181
GJ 1156	13.63	1.10	2994	iSHELL	3.62	0.20	2.93	0.52	136
GJ 644 C	6.07	0.68	2925	IGRINS	2.85	0.60	2.59	0.50	133
GJ 644 C	3.67	1.07	2925	iSHELL	2.05	0.42	2.12	0.39	120
GJ 752B	5.47	1.05	2500	IGRINS	1.32	0.50	1.15	0.33	93
GJ 752B	5.86	0.78	2500	iSHELL	1.12	0.26	1.17	0.39	145
GJ 1243	20.39	1.34	3328	IGRINS	3.99	0.43	3.64	0.28	180
GJ 1243	23.41	0.38	3328	iSHELL	3.86	0.14	3.09	0.33	160
GJ 803	10.99	1.50	3667	IGRINS	2.90	0.63	3.12	0.21	218
GJ 803	9.60	1.65	3667	iSHELL	3.49	0.41	3.29	0.09	110
GJ 873	3.18	1.18	3283	IGRINS	4.41	0.49	3.89	0.21	303
GJ 873	4.89	0.79	3283	iSHELL	3.79	0.33	4.83	0.12	200
GJ 388	6.05	1.34	3346	IGRINS	3.28	0.51	2.77	0.30	435
GJ 388	7.15	2.17	3346	iSHELL	4.30	0.42	3.85	0.25	130
GJ 569A	8.52	1.64	3600	IGRINS	1.79	0.41	1.02	0.80	259
GJ 569A	5.34	1.35	3600	iSHELL	1.84	0.22	1.37	0.23	260
Barta 161 12	42.61	2.43	3400	IGRINS	5.56	0.50	5.45	0.60	78
Barta 161 12	45.27	2.10	3400	iSHELL	4.77	0.52	5.74	0.23	160
G 80-21	6.53	1.84	3472	IGRINS	3.24	0.60	3.16	0.32	54
G 80-21	4.49	0.65	3472	iSHELL	3.53	0.36	2.66	0.21	60
GJ 182	15.36	2.32	3809	IGRINS	2.82	0.41	2.11	0.25	162
GJ 182	14.43	2.52	3809	iSHELL	3.56	0.36	3.29	0.09	60
GJ 3322	14.96	2.13	3235	IGRINS	3.30	0.35	2.29	0.15	118
GJ 3322	12.40	5.58	3235	iSHELL	2.64	1.55	2.84	0.80	60
GJ 208	4.78	0.52	3800	IGRINS	1.75	0.30	1.61	0.40	209
GJ 208	3.74	1.01	3800	iSHELL	1.85	0.70	1.42	0.10	175
GJ 3877	4.27	0.73	2996	IGRINS	2.33	0.71	1.84	0.70	88
GJ 3877	5.13	0.75	2996	iSHELL	2.96	0.32	2.40	0.14	90
V1274 Her	38.91	3.85	2931	IGRINS	6.03	0.70	5.66	1.34	100
V1274 Her	35.49	3.62	2931	iSHELL	6.16	0.64	6.15	1.35	160
G 227-22	9.46	0.70	3153	IGRINS	4.33	0.40	4.03	0.34	98
G 227-22	11.06	0.46	3153	iSHELL	4.01	0.50	5.44	0.19	98
GJ 4053	17.98	2.17	3300	IGRINS	2.37	0.60	2.57	0.40	152
GJ 4053	15.49	0.28	3300	iSHELL	1.57	0.74	1.44	0.63	160
GJ 1227	5.07	0.68	3202	IGRINS	0.87	0.3	0.85	0.13	161
GJ 1227	4.69	0.95	3202	iSHELL	…	…	0.48	0.07	140
GJ 9799	14.81	1.26	3493	IGRINS	3.90	0.30	3.06	0.23	96
GJ 9799	12.86	2.60	3493	iSHELL	3.85	0.27	3.24	0.22	270
GJ 896A	13.86	0.99	3351	IGRINS	3.81	0.30	3.07	0.22	136
GJ 896A	13.53	2.02	3351	iSHELL	3.76	0.80	3.91	0.26	200
GJ 896B	18.13	1.71	3178	IGRINS	4.77	0.74	4.76	0.60	136
GJ 896B	20.32	3.56	3178	iSHELL	5.02	0.44	3.63	0.17	155

Note. The S/N are for the *K*-band spectra for the IGRINS data, which are given by the IGRINS pipeline. The S/Ns of iSHELL data are given by the "Quicklook" spectral extraction during observations.

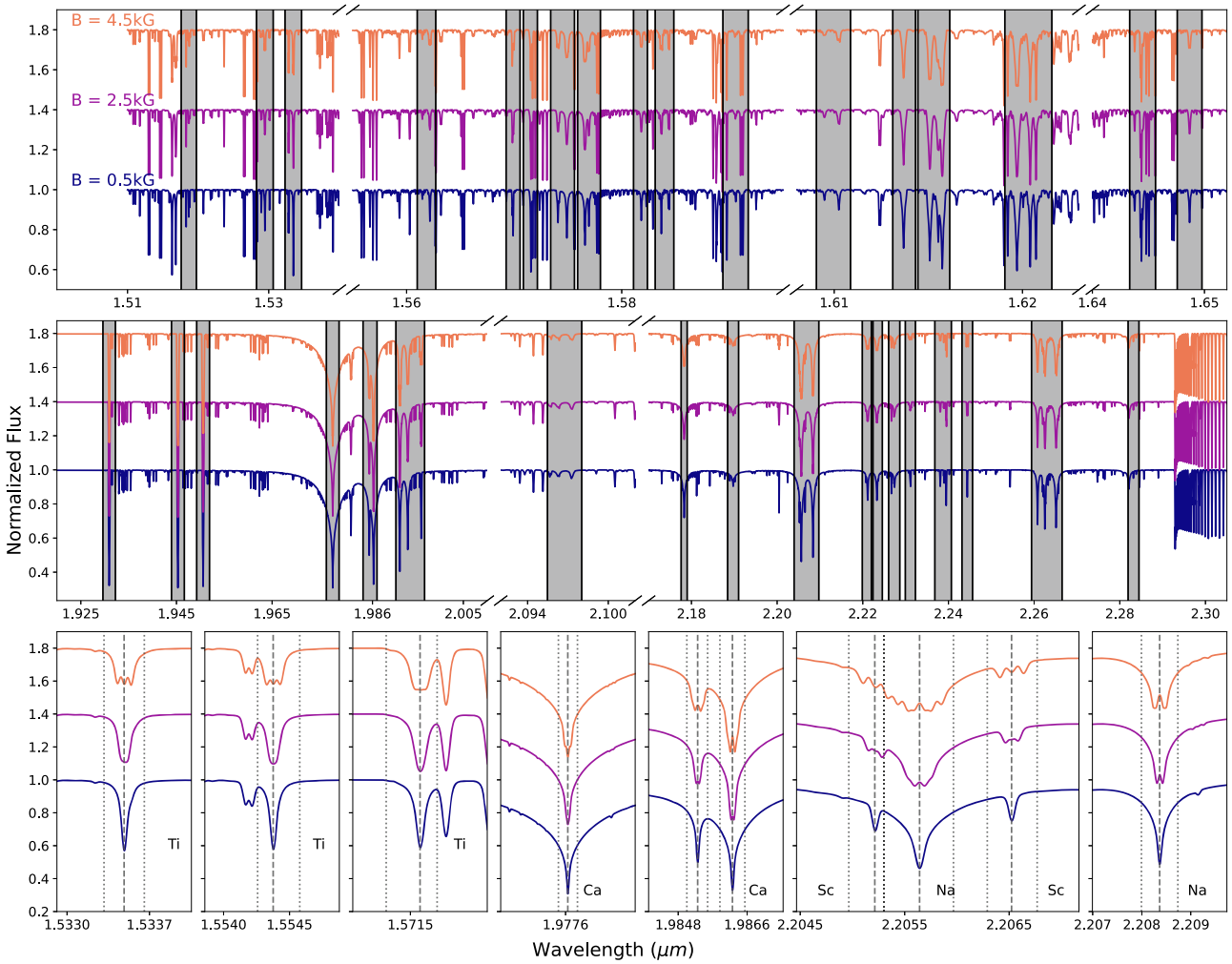

Figure 4. A sample plot of the MOOGStokes models that were used to build the EW-B field relationships. The top and the middle rows show the MOOGStokes models covering parts of the IGRINS *H* and *K* band, respectively. The grayed regions mark the atomic lines of interest. The bottom panels are the zoomed-in plots of a selection of atomic lines. The dashed lines indicate the location of the line center and the dotted lines around the dashed lines indicate the boundaries used to calculate the EW. The model parameters shown in the plot are $T_{\rm eff} = 3300$ K, $v\sin i = 0$ km s^{-1}, and $B = 0.5$, 2.5, and 4.5 kG.

the EW-B relations. When selecting the wavelength boundaries, we compared the MOOGStokes models with BT-Settl models (Allard et al. 2012), with the same stellar parameters (metallicity, $T_{\rm eff}$, and $\log g$) to ensure that the boundaries were not too wide to include other nearby lines or too narrow to exclude the wings of the lines when rotationally broadened. The boundaries marked in Figure 4 are fixed throughout the MOOGStokes models over all magnetic field strengths. The effect of magnetic field strengths on the magnetically sensitive atomic lines is obvious.

Previous studies have used the Fe I at 1.56 μm, Na I at 2.21 μm, or Ti I at 2.22 μm in investigating stellar magnetism (e.g., Saar & Linsky 1985; Johns-Krull et al. 1999; Johns-Krull & Valenti 2001), but not all three. With the wide spectral coverage of IGRINS, all three lines are observed simultaneously. In addition to these lines, we searched through the VALD database to identify as many magnetically sensitive spectral lines as possible. We found five (Groups 1–5) and eight (Groups 6–13) sets of atomic lines in the *H* and *K* bands, respectively, which are listed in Table 2. Note that there are two groups in the *H* band that involve Fe I lines, as those lines arise from different upper and lower states.

4.2.1. Building the EW-B Relations Using MOOGStokes Models

We first built the EW ratio to magnetic field relations (hereafter EW-B relations). Using ratios of EW's of magnetic field sensitive lines to related but less sensitive lines is less fraught than using the EW alone because it reduces the impact of small misestimations of stellar parameters. This approach is possible because each group of lines arises from the same atomic species with the same upper and lower transition states but with different $g_{\rm eff}$ and $\log gf$ values. This means that the atomic lines in the same group respond to the stellar parameters including $v\sin i$, $\log g$, and $T_{\rm eff}$ in the same way, except to the magnetic field strength (times the statistical weight), which allows us to minimize any degenerate effect on the EW from parameters other than the magnetic field. We excluded any line with $\log gf$ less than -2.5 and line depths less than 0.1 from each atomic group because it is challenging to distinguish those lines from the spectral noise.

For a given set of $T_{\rm eff}$ and $v\sin i$ MOOGStokes models, we measured the EW of all lines and searched for the line with the smallest enhancement with respect to 0 kG while changing the magnetic field strength in each group. Those lines are marked with the *sign next to their wavelengths in Table 2. For each

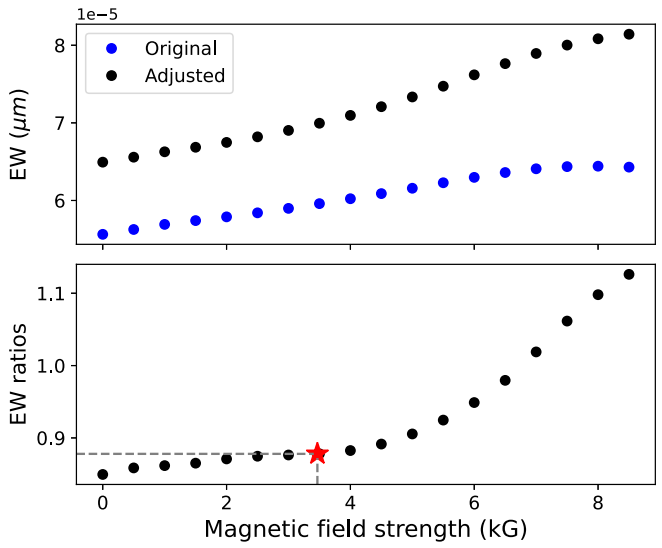

Figure 5. A sample plot of the Ti line showing how its EW and EW ratio changes as a function of the magnetic field strengths. The upper panel shows the measured Ti EWs from MOOGStokes (in blue) and the adjusted EWs (in black) using the residual EWs. The bottom panel shows the EW-B relation of the same Ti line using the adjusted EWs. The red star indicates the measured EW ratio from observation and its corresponding magnetic field strength.

group of atomic lines, we calculated the fractional increase of the EW of each line over the *marked line as a function of magnetic field strength to build the EW-B relations. This process is very similar to building the "magnetic curve-of-growth" from Basri et al. (1992) where they measured the fractional increase of the EW over the 0 kG case of the same line as a function of the magnetic field strength.

After building the EW-B relations of each group for various $T_{\rm eff}$ and $v\sin i$ MOOGStokes models, we applied the same procedures to the observed IGRINS and iSHELL spectra. For this task, we took the stitched, normalized, and radial velocity-shifted IGRINS and iSHELL spectra that were used for Zeeman broadening measurements. The wavelength regions making up the numerator and denominator of the EW ratio were defined by the MOOGStokes selections described in the previous paragraph.

4.2.2. Adjustment to the EW-B Relations

Since our method of building the EW-B relations is model dependent, we had to account for the difference between the MOOGStokes models and the observed spectra. To do so, we created "residual" spectra for each observed spectrum by subtracting MOOGStokes synthetic spectra from the observed spectrum. We then calculated the EWs of the residual spectrum ($\rm EW_{residual}$). Afterward, we calculated "adjusted" MOOGStokes EWs by adding the residual EWs to the original MOOGStokes EWs, $\rm EW_{adjusted} = EW_{original} + EW_{residual}$ (see the upper panel of Figure 5). Using these "adjusted" EWs, we then constructed the "adjusted" EW-B relations. These adjustments encapsulate systematic uncertainties by converting the empirical EW measurement onto the model EW scale.

4.2.3. Translating the EW Ratios to Magnetic Field Strengths

Once we had calculated the individual EWs and the EW ratios of the lines for each group of the observed spectrum, we translated those empirical measurements into the B field strengths using the adjusted EW-B relations (see the bottom panel of Figure 5). We adopted the weighted average and the weighted standard deviation of measurements for the final value and uncertainty we report. The weights are set to the product of $g_{\rm eff}$, $\log gf$, and the number of Zeeman components with typical values of 2–4. Figures 6 and 7 show the sample Zeeman intensification measurements of GJ 388 using the IGRINS *H*- and *K*-band spectra. In each figure, the top panel shows the position of each atomic line that is used in the measurements. The smaller bottom panels are a zoom-in view of the individual line. The dashed line is the central wavelength of each atomic line and the dotted lines are the boundaries used to measure the EW.

4.2.4. Systematics of the Method

Our approach to the Zeeman intensification method relies heavily on the accuracy of the models and measured EW of spectral lines, which are affected by a number of parameters other than the magnetic field strength. In this section, we briefly explain what they are and how we took care of each systematic.

The first parameter is the atomic abundance. To eliminate the effect of abundance on the EW, we looked at the ratios of EWs of pairs of atomic lines with small and large $g_{\rm eff}$ values of the same species.

The second parameter is $T_{\rm eff}$. To minimize the effect of $T_{\rm eff}$, we took the ratios of EWs of the set of atomic lines arising from the same lower and upper states.

The third parameter is $\log g$. To test the effect of $\log g$ in the magnetic field measurements, we translated our science EW ratios into magnetic field strengths also using EW-B relations of $\log g = 4.5$ and 5.5 dex. The measured magnetic field strengths changed within 0.2 kG when compared to the EW-B relations of $\log g = 5.0$ dex, which is smaller than our typical measurement error. Therefore, we conclude that the effect of $\log g$ is negligible.

The fourth parameter is $\log gf$. Because our method is semi-empirical, the effect of inaccurate $\log gf$ in generating the MOOGStokes models and hence building the EW-B relations introduces errors in our measurements. However, any effect of inaccurate $\log gf$ is random and is taken care of through the residual spectra.

The last parameter is the boundaries to calculate the EW of each line. We tested the significance of the boundary locations to the measured magnetic field strengths. For each line, we varied the boundary locations up to 15% and repeated the measurements. The measured magnetic field strengths changed within 0.3 kG for most lines. We rejected any line that is significantly affected by the location of the boundary due to the blending with adjacent lines.

5. Analysis and Results

We measured the average magnetic field strengths of 28 M dwarfs using the Zeeman broadening and intensification methods. Table 3 shows our measurements from the combined *H* and *K* bands using both methods for each object. For the individual IGRINS *H*- and *K*-band measurements, see Table 4 in the Appendix. Before we compare measurements from Zeeman broadening and Zeeman intensification using the IGRINS spectra, we discuss the details of underlying assumptions in each method and their impact on our measurements.

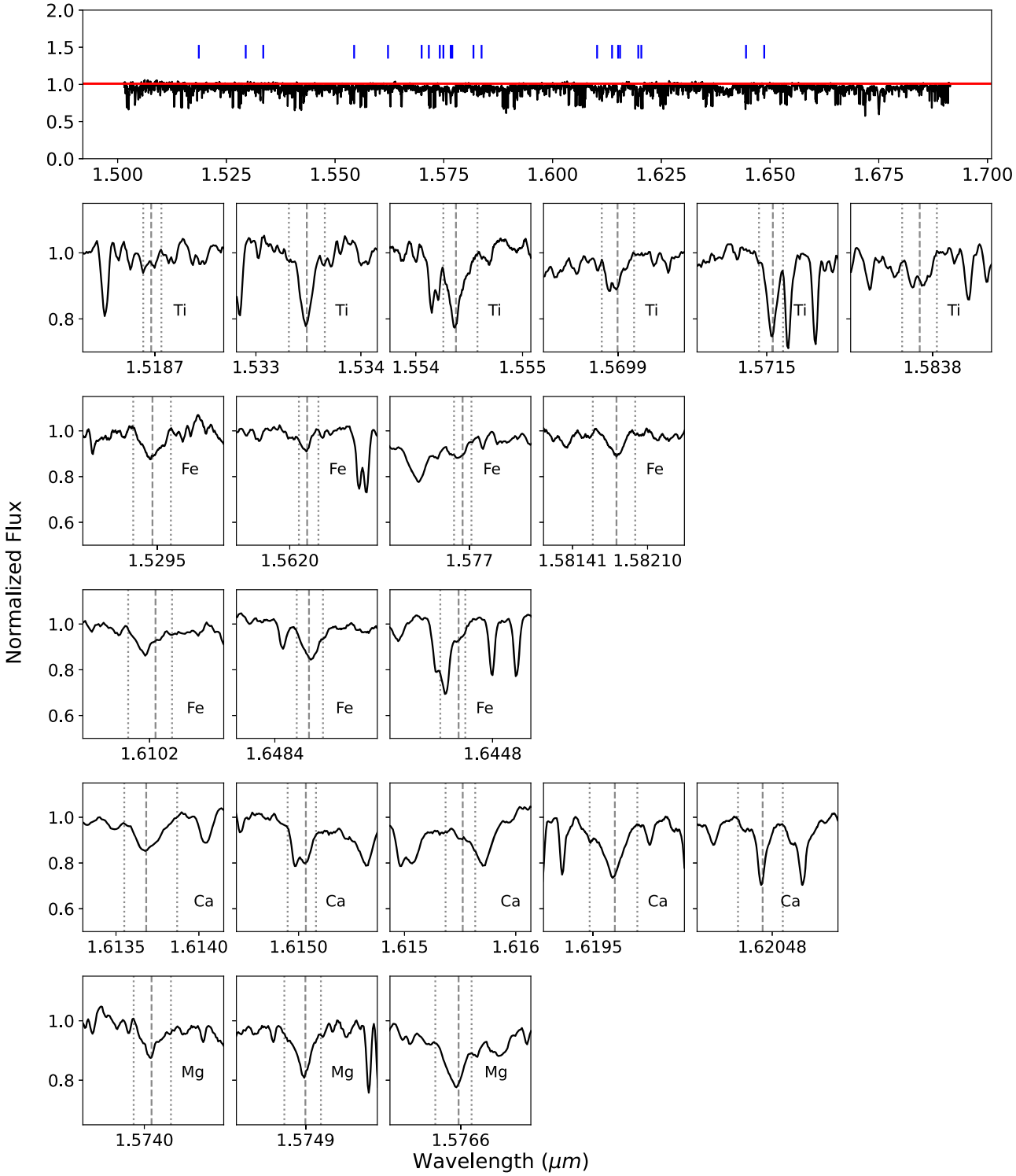

Figure 6. Sample Zeeman intensification measurements of GJ 388 using the IGRINS *H*-band spectrum. The top panel shows the position of each atomic line (in blue) that is used in the measurements. The continuum level is marked with a solid red line. The smaller bottom panels are the zoom-in view of the individual line. The dashed line is the central wavelength of each atomic line and the dotted lines are the boundaries used to measure the EW.

The Zeeman broadening method measures splitting into the spectral lines using Equations (2) and (3). These equations give the strengths of magnetic fields that are pointing directly toward the observer. Therefore, any other field configuration will result in less splitting of spectral lines. Because the true magnetic fields are in more complicated geometries, while we measure only the field component in the line of sight, what we measure from the stellar spectrum using these equations is the minimum disk-averaged magnetic field strength of the star.

The Zeeman intensification method is a semi-empirical approach that relies on the underlying assumptions and the accuracy of the synthetic MOOGStokes spectra. As mentioned in Section 4.2, MOOGStokes assumes a purely radial profile of

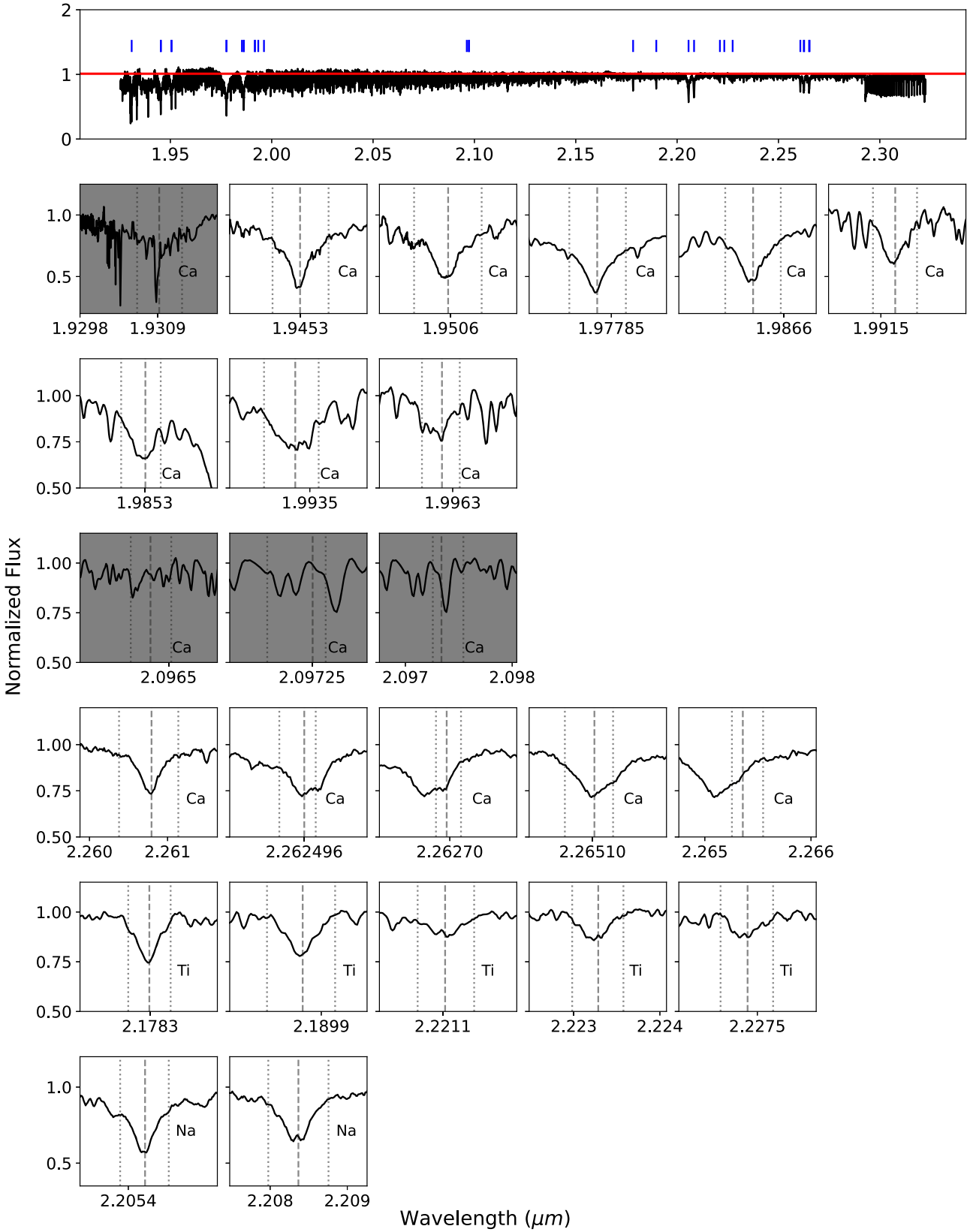

Figure 7. The same plot as in Figure 6 but for the *K*-band spectrum. The grayed panels are excluded from the measurement due to the bad quality of the data.

magnetic fields that are uniform in strength over the entire stellar surface. Therefore, the precomputed EW-B relations from MOOGStokes are based on a single-component magnetic field strength, averaged across the surface.

5.1. Comparison of Measurements from Zeeman Broadening and Intensification

Noting the embedded assumptions of each method, we first compare the measurements from the IGRINS *H* and *K* band for

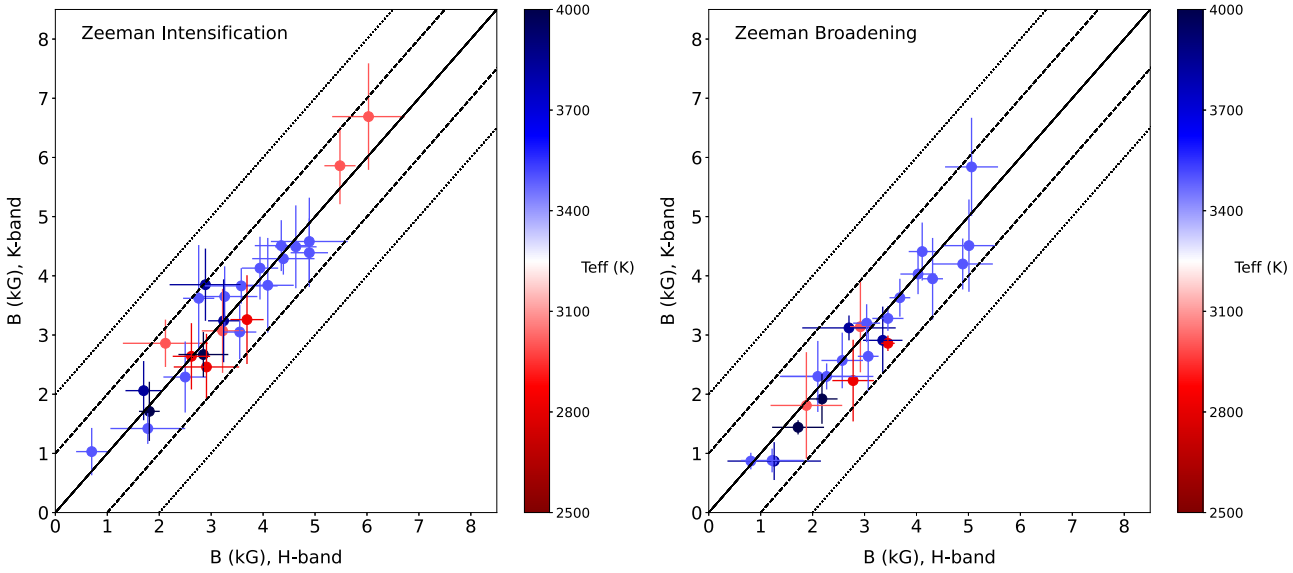

Figure 8. Comparison between the measured magnetic field strengths from IGRINS *H*- and *K*-band spectra. The left panel shows the measurements using the Zeeman intensification method and the right panel shows the measurements using the Zeeman broadening method. In both panels, solid black lines mark the 1-to-1 relations, and dashed and dotted lines mark 1 and 2 kG offsets. Different colored circles represent $T_{\rm eff}$ for the individual stars.

each method (Figure 8). The left and right panels show *K*- versus *H*-band measurements from the Zeeman intensification and Zeeman broadening methods, respectively. Different colors represent different $T_{\rm eff}$ of individual objects. For both methods, the *H*- and the *K*-band measurements are consistent, within ± 1 kG for a large range of $T_{\rm eff}$. Since the answers are consistent, we can improve consistency and reliability by combining the two results. Therefore, we present magnetic field measurements from *H* and *K* bands combined. To combine the *H*- and the *K*-band measurements, we took the distribution of measurements from both bands and calculated the weighted mean and weighted standard deviation as was done for the individual band measurements.

One clear difference between the two methods is the smaller number of measurements using Zeeman broadening for stars with $T_{\rm eff} < 3100$ K. This difference is due to the inability to measure Zeeman broadening in the *H* band as the spectrum becomes dominated by molecular lines and as atomic lines weaken, making it difficult to accurately measure the broadening. Although the same factors (e.g., molecular line blanketing and weaker atomic lines) also make the intensification method harder at lower temperatures, the intensification method is less affected. This result demonstrates an advantage of the Zeeman intensification method over the broadening method when studying cool, late-M dwarfs or brown dwarfs.

We compare the measurements with the intensification method versus those with the broadening method in Figure 9. The Zeeman intensification method results in slightly larger magnetic field strengths than the Zeeman broadening method in the majority of cases, regardless of whether the measurement is from the *H* or the *K* band, which is expected since the broadening method gives the minimum disk-average magnetic field strength. We calculated the best-fit relation between the two measurements where the slope and the *y*-intercept are 1.05 ± 0.05 and 0.26 ± 0.03, respectively (Figure 9). With the MOOGStokes models assuming a purely radial field configuration and the intensification method being model dependent, these offsets relate to the geometrical effect of sin*i* and the magnetic field orientations.

As mentioned in Section 3, for the Zeeman intensification method we measured the magnetic fields using both the literature $T_{\rm eff}$ and the calculated $T_{\rm eff}$ using the color–$T_{\rm eff}$ relations from Mann et al. (2015). In the cases of GJ 208, GJ 3379, GJ 285, GJ 1156, GJ 4053, GJ 1243, and GJ 9799, the $T_{\rm eff}$ differences are between 100 and 200 K and we find that the measurements are consistent within the uncertainties regardless of the whether we use the EW-B relation for one $T_{\rm eff}$ or the other. In the case of GJ 752B, Shulyak et al. (2019) report 2500 K but the $T_{\rm eff}$ calculated using the color–$T_{\rm eff}$ relation from Mann et al. (2015) gives 3200 K. We find that the EW-B relation from 2500 K gives consistent magnetic field strength with the literature and we adopt this as the final value. We suspect the large discrepancy in the $T_{\rm eff}$ for GJ 752B is due to erroneous *V*, *J*, and *H* magnitudes used in the color–$T_{\rm eff}$ relation, where the magnitudes may have been for the parent GJ 752 system and not for GJ 752B. In the case of GJ 644 C, we tried three $T_{\rm eff}$ values: 2600 K from Shulyak et al. (2019), 2900 K from Mann color–$T_{\rm eff}$, and 3000 K from Reiners et al. (2022). We find that the EW-B relations from 2900 and 3000 K give a consistent measurement within the uncertainties. The 2600 K magnetic field strengths are off by 3σ from the literature value. In summary, we have adopted the literature $T_{\rm eff}$ values to choose the EW-B relation, except when there are multiple $T_{\rm eff}$ values reported, in which case we adopt the calculated $T_{\rm eff}$ using the color–$T_{\rm eff}$ relations from Mann et al. (2015).

5.2. Comparison to Literature Magnetic Field Strengths

We compare our *B*-field measurements with the literature values, which are shown in Figure 10. All magnetic field measurements from the literature are done through detailed line profile modeling. These measurements are based on the assumption that there is a distribution of magnetic field components, each covering a part of the stellar surface with a filling factor. A majority of the literature measurements are based on multicomponent magnetic field strengths except those from Afram et al. (2009) and Shulyak et al. (2011). The panels in Figure 10 show the literature comparison to our

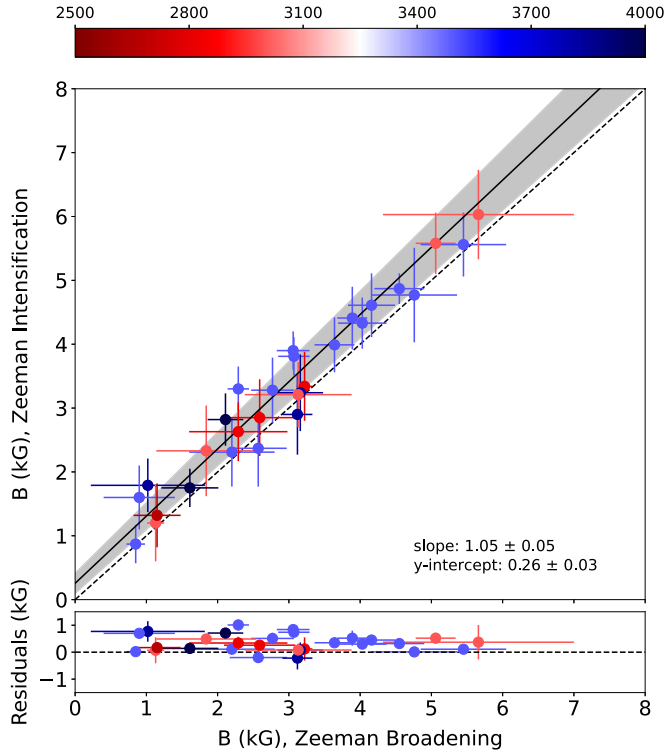

Figure 9. Comparison between the magnetic field strengths measured by the Zeeman broadening and Zeeman intensification methods. The solid black line represents the best-fit relation between the two measurements with the 1σ uncertainty regime in gray, and the dashed line marks the 1-to-1 relation.

measurements from the Zeeman intensification and Zeeman broadening methods. We colored each measurement based on the S/N per resolution element of the IGRINS spectra, with orange representing S/N $\geqslant$ 150 while green representing S/N $<$ 150. Filled symbols represent the targets with $v\sin i < 15$ km s^{-1} and empty symbols represent the targets with $v\sin i \geqslant 15$ km s^{-1}. The solid black line marks the 1-to-1 relation, and the dashed and the dotted lines mark 1 and 2 kG offsets, respectively. We find that the measurements from both the Zeeman broadening and Zeeman intensification methods are consistent with the reported magnetic field strengths from the literature to well within $\pm$1 kG around the 1-to-1 line for most of the targets, with an average offset of -0.17 kG for the broadening method and $+0.19$ kG for the intensification method. For both methods, the larger difference from the literature values could be attributed to a combined effect from lower S/N, higher $v\sin i$, and different epochs of observations. At higher $v\sin i$, Zeeman broadening method becomes less sensitive and the effective S/N for the EW measurements goes down as the spectral line gets wider.

5.3. Data Requirements for Robust Magnetic Field Strength Measurements

The primary goal of this work is to explore the limitations and the accuracy of magnetic field measurements using IGRINS spectra, since we wish to use them to determine the magnetic field strengths of over 500 M dwarfs in the IGRINS archive (RRISA; Sawczynec et al. 2022). For optical wavelength observations, Kochukhov (2021) pointed out the need for high-resolution ($R \geqslant 50{,}000$, ideally $\sim 10^5$) spectra for detailed line profile modeling of Zeeman broadening and lower resolution ($R \sim 30{,}000$) spectra for Zeeman intensification measurements. Previous studies that report the magnetic field strengths of our sample have been done using optical spectra and used Zeeman broadening or the line profile fitting method. Combining the fact that the spectral resolution of IGRINS is lower than the suggested $R \geqslant 50{,}000$, and that our measurements from Zeeman broadening are consistent with the literature (within the expected offsets), demonstrates the advantage of using near-infrared spectra. This is an expected result given that M dwarfs are intrinsically brighter in the near-infrared and given the λ^2-dependence of the Zeeman effects.

To estimate the weakest magnetic field strength that can be measured from the Zeeman intensification method, we added Gaussian random noise to MOOGStokes models to best represent the desired S/Ns of IGRINS spectra. We were able to recover a model magnetic field strength as low as $\sim$0.7 kG with an S/N $\sim$200 spectrum and $\sim$0.8 kG with an S/N $\sim$150 spectrum. These S/Ns also permitted measurements of magnetic fields using the broadening method that is close to the instrumental broadening of IGRINS, which is $\sim$0.9 kG. In fact, the weakest magnetic fields detected from our methods are 0.87 ± 0.30 kG with the intensification method and 0.85 ± 0.13 kG with the broadening method, both from an S/N $\sim$160 spectrum. These results demonstrate that we need at least S/N $\gtrsim$150 to reliably measure the magnetic field strengths from both the Zeeman intensification and Zeeman broadening methods.

To explore the limitations in measurements from IGRINS in terms of the spectral resolution, we compare measurements from the Zeeman broadening method, which is known to be more sensitive to the quality of the data than the Zeeman intensification method (e.g., Kochukhov 2021). We validate and compare the IGRINS results with the iSHELL observations analyzed with the same methods. In Figure 11, we plot the detected magnetic field strength from IGRINS against that from iSHELL and CARMENES. Because the iSHELL spectra we have only cover the K band, for this comparison we chose the IGRINS K-band Zeeman broadening measurements only, which are shown in the left panel in Figure 11. Measurements from the two spectrographs are consistent well within $\pm$1 kG around the 1-to-1 line for all targets. Furthermore, iSHELL was able to detect magnetic field strengths that are a few tenths of a kG smaller than IGRINS, which is as expected given the higher resolution of iSHELL. For the comparison with the CARMENES measurements, all of which are based on the multicomponent line fitting method, we use the combined IGRINS H- and K-band measurements. We cross matched our sample with those from Shulyak et al. (2019) and Reiners et al. (2022), which are shown in the middle panel. The right panel is the comparison between iSHELL and CARMENES measurements. We point out one obvious limitation related to the relatively lower resolution of IGRINS; field strengths $<$ $\sim$0.9 kG are beyond the reach of IGRINS observations when using the Zeeman broadening method, consistent with the instrumental broadening limit. We also point out that the offsets of the IGRINS and the iSHELL ($R \sim 75{,}000$) measurements using our methods and the CARMENES ($R \sim 80{,}400$) measurements are, as expected, lower, given the underlying assumption of the Zeeman broadening method we used.

To summarize, it is quite obvious but important to point out that the accuracy of measurements is dominated by the spectral

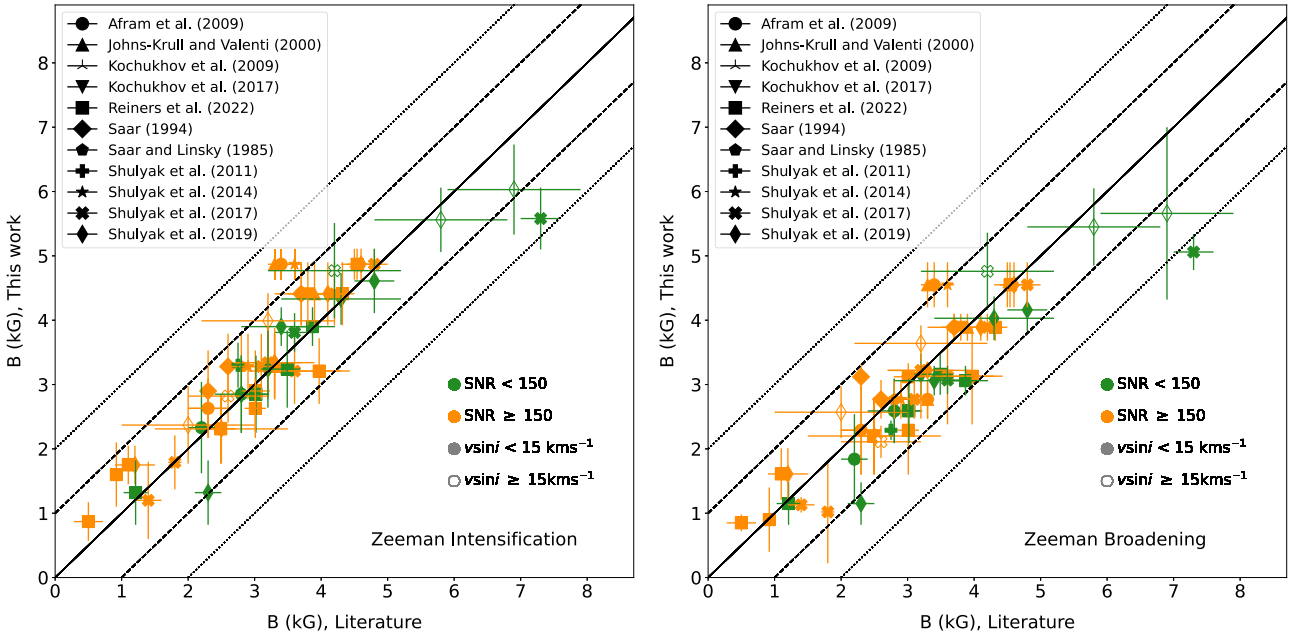

Figure 10. Comparison between the measured magnetic field strengths from this work and literature values. The left panel shows the magnetic field measurements from the Zeeman intensification method vs. those from the literature, while the right panel shows the measurements from the Zeeman broadening method. The solid black lines mark the 1-to-1 relations and dashed and dotted lines mark 1 and 2 kG offsets.

resolution whereas the precision of measurements is dominated by the S/N of a spectrum. Therefore, given that the spectral resolution of IGRINS is fixed at $R = 45{,}000$ and the S/N being the only variable in terms of the quality of data, we set S/N $\gtrsim$150 as a requirement for all our future studies of stellar magnetism.

6. Discussion

The value of this work lies in the magnetic field measurements from both Zeeman intensification and broadening simultaneously. Previous studies have only used either one of the two methods due to the limited number of atomic lines that are suitable for both methods. Thanks to the wide wavelength coverage of IGRINS, which provides a rich set of atomic lines, we can use both methods to measure the magnetic fields of M dwarfs. We find that the Zeeman intensification and Zeeman broadening methods are complementary to each other in that they allow us to cross check the accuracy of the measurements for objects with $v\sin i \leqslant 15$ km s^{-1}. We also stress that the magnetic fields measured by both methods only provide the time-averaged global surface magnetic field strengths, which are not the same as a magnetic field strength at a localized point at a given time.

Although we use the EW ratios rather than the EWs themselves, to avoid any systematic of the MOOGStokes or the MARCS models, three caveats still apply to our method. One is related to the model-dependent nature of the Zeeman intensification method. Our measurements are limited by the accuracy and the availability of the MARCS models used to build the EW-B relations as well as by the assumptions made by MOOGStokes. For instance, the MARCS model does not fully cover the entire M dwarf $T_{\rm eff}$ range, excluding M dwarfs with $T_{\rm eff} < 2500$ K from the analysis. In addition, MARCS models are nonmagnetic atmospheric models and lack a detailed handling of changes in the thermodynamic structure given the magnetic field. The other caveat when using the EW ratio is, if the atomic line that is used in the denominator to set the base of the "magnetic curve-of-growth" is noisy, the overall ratio measurements and hence the translation into magnetic field strength will be noisy as well. We carefully inspected all spectra and excluded any measurement from the same atomic group if the spectral line assigned as the denominator had a lower S/N than the other lines in the group. Lastly, the placement of the continuum level affects the overall accuracy of the magnetic field measurement where an underestimated continuum weakens the weak lines more than the strong lines, resulting in an inaccurate EW ratio measurement. We inspected individual spectra to ensure that the continuum level was placed as accurately as possible. However, defining the continuum level for M dwarfs is challenging and any offset in the continuum placement may add uncertainties in the magnetic field measurement.

7. Conclusions

IGRINS is one of a few high-resolution spectrographs that offers broad coverage in the near-infrared H and K bands. In this paper, we investigated the capabilities and limitations of magnetic field measurements from the IGRINS spectra using the Zeeman intensification and Zeeman broadening methods. These methods provide direct measurements of average magnetic field strengths on the surface of M dwarfs. We measured the magnetic field strengths of 28 M dwarfs and found that the intensification method measures a magnetic field strength that is comparable to what the broadening method measures. Although the magnetic field strengths from the intensification method are slightly larger by 0.18 ± 0.04 kG than the broadening method, this is an expected result given the embedded assumptions discussed in Section 5 that Zeeman broadening method provides a disk-averaged minimum magnetic field strength on the stellar surface. We also find that most

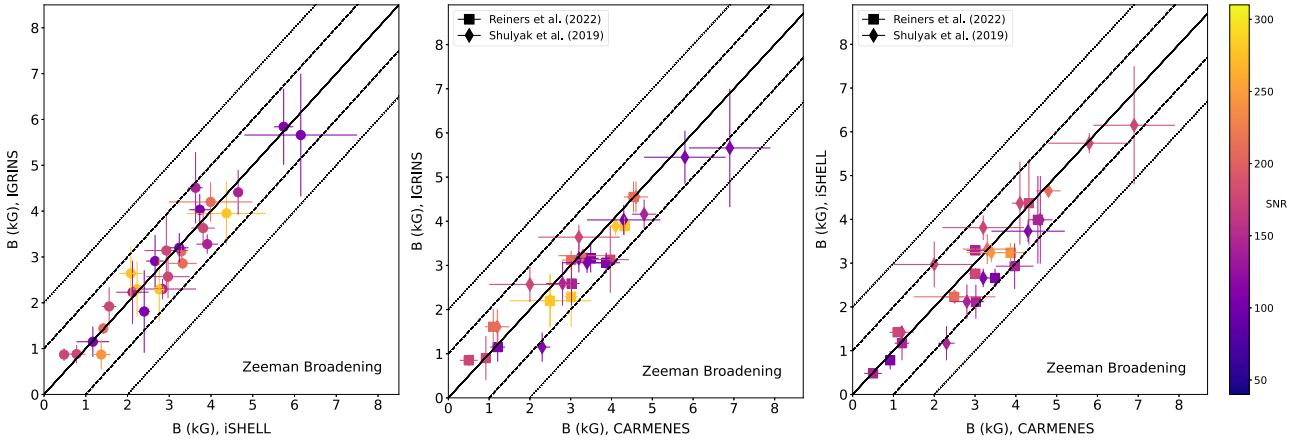

Figure 11. Comparison between the measured magnetic field strengths derived from IGRINS with those derived from iSHELL and CARMENES data. Solid black lines mark the 1-to-1 relations and dashed and dotted lines mark 1 and 2 kG offsets. Different colors represent the S/N of each IGRINS (left and middle panels) and iSHELL (right panel) spectrum from the present study.

of our measurements from both methods are in good agreement with the reported magnetic field strengths from the literature considering the various methods, resolutions of spectra, and wavelengths employed. By comparing the measurements from IGRINS with those from higher resolution spectrographs, iSHELL and CARMENES, we determine the required S/N for future studies on stellar magnetism to be $\gtrsim$150. With this condition, we are able to measure the magnetic field strength as weak as $\sim$0.9 kG with the Zeeman broadening method and $\sim$0.7–0.8 kG with the Zeeman intensification method.

The Zeeman broadening method is great in the sense that it is purely empirical. However, this method is only applicable to stars with low $v\sin i$. On the other hand, the Zeeman intensification method is insensitive to $v\sin i$ and therefore is accessible to stars with high $v\sin i$. However, this method requires a large number of both strong and weak lines to reliably measure the magnetic field strength. Moreover, the Zeeman intensification method is model dependent and requires reliable models, which is difficult to find across all the parameter space spanned by M dwarfs. In the context of studying stellar magnetism, we find that the power of IGRINS spectra in determining the stellar surface magnetic field strengths is threefold. The first is related to IGRINS being a near-infrared spectrograph where the magnitude of the Zeeman effect increases with λ^2. This wavelength dependence allows us to measure lower magnetic field strengths than at optical wavelengths. The second is related to IGRINS' large wavelength coverage and high spectral resolution. We are improving the way the Zeeman intensification method works and are able to measure the magnetic field strengths through the intensification method better than previous measurements with lower resolution or with less wavelength coverage. Lastly, with IGRINS spectra, we are able to use both the Zeeman intensification and Zeeman broadening methods simultaneously.

We thank the anonymous referee whose comments and suggestions helped improve and clarify this manuscript. We thank Maryam Hussaini for her investigation of magnetic field effects on M dwarf spectra while an undergraduate at the University of Texas at Austin. We acknowledge the work of Dr. Kimberly Sokal to develop the normalizing and order stitching scripts employed in this work. R.L.V. acknowledges support from CONACYT through a postdoctoral fellowship within the program Estancias Posdoctorales por México. This work used the Immersion Grating Infrared Spectrometer (IGRINS) that was developed under a collaboration between the University of Texas at Austin and the Korea Astronomy and Space Science Institute (KASI) with the financial support of the Mt. Cuba Astronomical Foundation, of the US National Science Foundation under grants AST-1229522 and AST-1702267, of the McDonald Observatory of the University of Texas at Austin, of the Korean GMT Project of KASI, and Gemini Observatory. These results made use of the Lowell Discovery Telescope (LDT) at Lowell Observatory. Lowell is a private, nonprofit institution dedicated to astrophysical research and public appreciation of astronomy and operates the LDT in partnership with Boston University, the University of Maryland, the University of Toledo, Northern Arizona University, and Yale University. This work has made use of the VALD database, operated at Uppsala University, the Institute of Astronomy RAS in Moscow, and the University of Vienna. This paper includes data taken at The McDonald Observatory of The University of Texas at Austin. This work used iSHELL at the Infrared Telescope Facility, which is operated by the University of Hawaii under contract 80HQTR19D0030 with the National Aeronautics and Space Administration. This material is based upon work supported by the National Science Foundation under grant No. AST-1908892 to G. Mace.

Facilities: Harlan J. Smith (IGRINS), LDT (IGRINS), IRTF (iSHELL).

Software: `IGRINS pipeline` (Lee & Lin 2017), `spextool` (Cushing et al. 2004), `xtellcor` (Vacca et al. 2003), `MOOGStokes` (Deen 2013), `MARCS atmospheric model` (Gustafsson et al. 2008), `mpfit` (Markwardt 2009).

Appendix

We present magnetic field measurements for the individual IGRINS *H*- and the *K*-band measurements of each object in Table 4. As shown in the table, measurements from each band are consistent with the reported uncertainties. For the analysis, we combined individual *H*- and *K*-band measurements by calculating the weighted mean and standard deviation.

Table 4
Measured Magnetic Field Strengths for the Individual *H*- and *K*-band Spectra

Target	Instrument	Zeeman Intensification				Zeeman Broadening			
		B_H (kG)	$B_{H,err}$ (kG)	B_K (kG)	$B_{K,err}$ (kG)	B_H (kG)	$B_{H,err}$ (kG)	B_K (kG)	$B_{K,err}$ (kG)
GJ 51	IGRINS	4.63	0.40	4.49	0.70	4.11	0.26	4.41	0.49
GJ 3379	IGRINS	2.50	0.42	2.29	0.60	2.10	0.70	2.30	0.60
GJ 285	IGRINS	4.89	0.36	4.39	0.58	4.89	0.58	4.20	0.43
GJ 299	IGRINS	1.78	0.72	1.42	0.26	1.22	0.60	0.88	0.20
GJ 1111	IGRINS	3.69	0.32	3.26	0.75	3.45	0.13	2.86	0.13
GJ 3622	IGRINS	…	…	1.20	0.60	…	…	1.13	0.12
GJ 406	IGRINS	2.62	0.36	2.64	0.56	…	…	2.29	0.69
GJ 412B	IGRINS	5.48	0.30	5.86	0.65	…	…	5.06	0.28
GJ 1156	IGRINS	3.22	0.40	3.07	0.71	2.92	0.20	3.14	0.77
GJ 644 C	IGRINS	2.91	0.63	2.46	0.56	2.78	0.40	2.23	0.69
GJ 752B	IGRINS	…	…	1.32	0.50	…	…	1.15	0.33
GJ 1243	IGRINS	3.94	0.35	4.13	0.53	3.68	0.20	3.63	0.32
GJ 803	IGRINS	2.89	0.69	3.85	0.61	2.70	0.90	3.12	0.21
GJ 873	IGRINS	4.35	0.53	4.51	0.43	4.31	0.20	3.95	0.69
GJ 388	IGRINS	3.26	0.63	3.65	0.51	3.07	0.20	2.64	0.59
GJ 569A	IGRINS	1.70	0.35	2.06	0.50	1.26	0.90	0.87	0.32
Barta 161 12	IGRINS	…	…	5.56	0.50	5.06	0.51	5.84	0.83
G 80-21	IGRINS	3.24	0.30	3.24	0.70	3.35	0.38	2.91	0.57
GJ 182	IGRINS	2.85	0.48	2.67	0.38	2.18	0.30	1.92	0.42
GJ 3322	IGRINS	3.55	0.32	3.05	0.46	2.27	0.90	2.30	0.22
GJ 208	IGRINS	1.81	0.20	1.71	0.50	1.72	0.50	1.44	0.12
GJ 3877	IGRINS	2.12	0.82	2.86	0.40	1.88	0.69	1.81	0.90
V1274 Her	IGRINS	6.03	0.70	6.69	0.90	…	…	5.66	1.34
G 227-22	IGRINS	4.39	0.60	4.29	0.27	4.03	0.34	4.03	0.34
GJ 4053	IGRINS	2.76	0.30	3.62	0.90	2.57	0.40	2.57	0.47
GJ 1227	IGRINS	0.70	0.30	1.03	0.40	0.81	0.11	0.87	0.14
GJ 9799	IGRINS	4.09	0.50	3.84	0.80	3.04	0.26	3.20	0.32
GJ 896A	IGRINS	3.58	0.70	3.83	0.30	3.45	0.30	3.28	0.21
GJ 896B	IGRINS	4.89	0.74	4.58	0.74	5.01	0.50	4.51	0.78

ORCID iDs

Eunkyu Han https://orcid.org/0000-0001-9797-0019
Ricardo López-Valdivia https://orcid.org/0000-0002-7795-0018
Gregory N. Mace https://orcid.org/0000-0001-7875-6391
Daniel T. Jaffe https://orcid.org/0000-0003-3577-3540

References

Afram, N., Reiners, A., & Berdyugina, S. V. 2009, in ASP Conf. Ser. 405, Solar Polarization 5: In Honor of Jan Stenflo, ed. S. V. Berdyugina, K. N. Nagendra, & R. Ramelli (San Francisco, CA: ASP), 527
Allard, F., Homeier, D., & Freytag, B. 2012, Royal Society of London Philosophical Transactions Series A, 370, 2765
Astudillo-Defru, N., Delfosse, X., Bonfils, X., et al. 2017, A&A, 600, A13
Barnes, R., Meadows, V. S., Domagal-Goldman, S. D., et al. 2011, in ASP Conf. Ser. 448, 16th Cambridge Workshop on Cool Stars, Stellar Systems, and the Sun, ed. C. Johns-Krull, M. K. Browning, & A. A. West (San Francisco, CA: ASP), 391
Basri, G., & Marcy, G. W. 1994, ApJ, 431, 844
Basri, G., Marcy, G. W., & Valenti, J. A. 1992, ApJ, 390, 622
Berger, E. 2006, ApJ, 648, 629
Bochanski, J. J., Hawley, S. L., Covey, K. R., et al. 2010, AJ, 139, 2679
Brown, S. F., Donati, J. F., Rees, D. E., & Semel, M. 1991, A&A, 250, 463
Browning, M. K., Basri, G., Marcy, G. W., West, A. A., & Zhang, J. 2010, AJ, 139, 504
Chabrier, G. 2003, PASP, 115, 763
Chabrier, G., & Baraffe, I. 1997, A&A, 327, 1039
Chabrier, G., Gallardo, J., & Baraffe, I. 2007, A&A, 472, L17
Chabrier, G., & Küker, M. 2006, A&A, 446, 1027
Charbonneau, P. 2014, ARA&A, 52, 251
Cushing, M. C., Vacca, W. D., & Rayner, J. T. 2004, PASP, 116, 362
Deen, C. P. 2013, AJ, 146, 51
Delfosse, X., Forveille, T., Perrier, C., & Mayor, M. 1998, A&A, 331, 581
Dikpati, M., & Charbonneau, P. 1999, ApJ, 518, 508
Dittmann, J. A., Irwin, J. M., Charbonneau, D., & Newton, E. R. 2016, ApJ, 818, 153
Donati, J. F., & Brown, S. F. 1997, A&A, 326, 1135
Donati, J. F., Morin, J., Petit, P., et al. 2008, MNRAS, 390, 545
Donati, J. F., Semel, M., & Praderie, F. 1989, A&A, 225, 467
Dressing, C. D., & Charbonneau, D. 2013, ApJ, 767, 95
Durney, B. R., De Young, D. S., & Roxburgh, I. W. 1993, SoPh, 145, 207
Favier, B., & Bushby, P. J. 2013, JFM, 723, 529
Feiden, G. A., & Chaboyer, B. 2013, ApJ, 779, 183
Gaidos, E., Mann, A. W., Lépine, S., et al. 2014, MNRAS, 443, 2561
Gáspár, A., Rieke, G. H., & Ballering, N. 2016, ApJ, 826, 171
Gully-Santiago, M. A., Jaffe, D. T., Brooks, C. B., Wilson, D. W., & Muller, R. E. 2014, Proc. SPIE, 9151, 91515K
Gustafsson, B., Edvardsson, B., Eriksson, K., et al. 2008, A&A, 486, 951
Han, E., Muirhead, P. S., Swift, J. J., et al. 2017, AJ, 154, 100
Han, E., Muirhead, P. S., & Swift, J. J. 2019, AJ, 158, 111
Hardegree-Ullman, K. K., Cushing, M. C., Muirhead, P. S., & Christiansen, J. L. 2019, AJ, 158, 75
Hawley, S. L., Davenport, J. R. A., Kowalski, A. F., et al. 2014, ApJ, 797, 121
Henry, T. J., Jao, W.-C., Winters, J. G., et al. 2018, AJ, 155, 265
Hussaini, M., Mace, G. N., López-Valdivia, R., Honaker, E. J., & Han, E. 2020, RNAAS, 4, 241
Johns-Krull, C. M., & Valenti, J. A. 1996, ApJL, 459, L95
Johns-Krull, C. M., & Valenti, J. A. 2000, in ASP Conf. Ser. 198, Stellar Clusters and Associations: Convection, Rotation, and Dynamos, ed. R. Pallavicini, G. Micela, & S. Sciortino (San Francisco, CA: ASP), 371
Johns-Krull, C. M., & Valenti, J. A. 2001, ApJ, 561, 1060
Johns-Krull, C. M., Valenti, J. A., & Koresko, C. 1999, ApJ, 516, 900
Kesseli, A. Y., Muirhead, P. S., Mann, A. W., & Mace, G. 2018, AJ, 155, 225
Kochukhov, O. 2021, A&ARv, 29, 1
Kochukhov, O., Hackman, T., Lehtinen, J. J., & Wehrhahn, A. 2020, A&A, 635, A142
Kochukhov, O., Heiter, U., Piskunov, N., et al. 2009, in AIP Conf. Ser. 1094, 15th Cambridge Workshop on Cool Stars, Stellar Systems, ed. E. Stempels (Melville, NY: AIP), 124

Kochukhov, O., & Lavail, A. 2017, ApJL, 835, L4
Koenigl, A. 1991, ApJL, 370, L39
Landstreet, J. D. 1992, A&ARv, 4, 35
Lee, C.-H., & Lin, C.-C. 2017, RAA, 17, 15
Lee, J.-J., Gullikson, K., & Kaplan, K. 2017, igrins/plp v2.2.0, Zenodo, doi:10.5281/zenodo.845059
López-Valdivia, R., Mace, G. N., Han, E., et al. 2023, ApJ, 943, 49
MacDonald, J., & Mullan, D. J. 2013, ApJ, 765, 126
Mace, G., Kim, H., Jaffe, D. T., et al. 2016, Proc. SPIE, 9908, 99080C
Mace, G., Sokal, K., Lee, J.-J., et al. 2018, Proc. SPIE, 10702, 107020Q
Mann, A. W., Feiden, G. A., Gaidos, E., Boyajian, T., & von Braun, K. 2015, ApJ, 804, 64
Mann, A. W., Gaidos, E., Mace, G. N., et al. 2016, ApJ, 818, 46
Markwardt, C. B. 2009, in ASP Conf. Ser. 411, Astronomical Data Analysis Software and Systems XVIII, ed. D. A. Bohlender, D. Durand, & P. Dowler (San Francisco, CA: ASP), 251
Marsh, J. P., Mar, D. J., & Jaffe, D. T. 2007, ApOpt, 46, 3400
Moffatt, H. K. 1978, Cambridge Monographs on Mechanics and Applied Mathematics (Cambridge: Cambridge Univ. Press)
Mohanty, S., & Basri, G. 2003, ApJ, 583, 451
Morales, J. C., Gallardo, J., Ribas, I., et al. 2010, ApJ, 718, 502
Mouschovias, T. C., & Spitzer, L. J. 1976, ApJ, 210, 326
Moutou, C., Dalal, S., Donati, J. F., et al. 2020, A&A, 642, A72
Muirhead, P. S., Vanderburg, A., Shporer, A., et al. 2013, ApJ, 767, 111
Muirhead, P. S., Veyette, M. J., Newton, E. R., Theissen, C. A., & Mann, A. W. 2020, AJ, 159, 52
Neves, V., Bonfils, X., Santos, N. C., et al. 2013, A&A, 551, A36
Noyes, R. W., Hartmann, L. W., Baliunas, S. L., Duncan, D. K., & Vaughan, A. H. 1984, ApJ, 279, 763
Ossendrijver, M. 2003, A&ARv, 11, 287
Pallavicini, R., Golub, L., Rosner, R., et al. 1981, ApJ, 248, 279
Park, C., Jaffe, D. T., Yuk, I.-S., et al. 2014, Proc. SPIE, 9147, 91471D
Parker, E. N. 1955, ApJ, 122, 293
Parker, E. N. 1975, ApJ, 198, 205
Pizzolato, N., Maggio, A., Micela, G., Sciortino, S., & Ventura, P. 2003, A&A, 397, 147
Rayner, J., Tokunaga, A., Jaffe, D., et al. 2022, PASP, 134, 015002
Reid, I. N., & Hawley, S. L. 2005, New Light on Dark Stars Red Dwarfs, Low-Mass Stars, Brown Stars (Moscow: Praxis Publishing)
Reiners, A., & Basri, G. 2007, ApJ, 656, 1121
Reiners, A., & Basri, G. 2009, A&A, 496, 787
Reiners, A., & Basri, G. 2010, ApJ, 710, 924
Reiners, A., Shulyak, D., Käpylä, P. J., et al. 2022, A&A, 662, A41
Ryabchikova, T., Piskunov, N., Kurucz, R. L., et al. 2015, PhyS, 90, 054005
Saar, S. H. 1988, ApJ, 324, 441
Saar, S. H. 1994, in IAU Symp. 154, Infrared Solar Physics, ed. D. M. Rabin, J. T. Jefferies, & C. Lindsey (Tucson, AZ: Univ. Arizona Press), 493
Saar, S. H., & Linsky, J. L. 1985, ApJL, 299, L47
Sawczynec, E., Mace, G., Gully-Santiago, M., & Jaffe, D. 2022, AAS Meeting Abstracts, 54, 203.06
Schatzman, E. 1962, AnAp, 25, 18
Semel, M. 1989, A&A, 225, 456
Semel, M., Donati, J. F., & Rees, D. E. 1993, A&A, 278, 231
Shu, F., Najita, J., Ostriker, E., et al. 1994, ApJ, 429, 781
Shulyak, D., Reiners, A., Engeln, A., et al. 2017, NatAs, 1, 0184
Shulyak, D., Reiners, A., Nagel, E., et al. 2019, A&A, 626, A86
Shulyak, D., Reiners, A., Seemann, U., Kochukhov, O., & Piskunov, N. 2014, A&A, 563, A35
Shulyak, D., Seifahrt, A., Reiners, A., Kochukhov, O., & Piskunov, N. 2011, MNRAS, 418, 2548
Sneden, C. A. 1973, PhD thesis, The Univ. of Texas at Austin
Soderblom, D. R., Stauffer, J. R., Hudon, J. D., & Jones, B. F. 1993, ApJS, 85, 315
Stewart, R. T., Innis, J. L., Slee, O. B., Nelson, G. J., & Wright, A. E. 1988, AJ, 96, 371
Stix, M. 1981, SoPh, 74, 79
Tsuji, T., & Nakajima, T. 2014, PASJ, 66, 98
Vacca, W. D., Cushing, M. C., & Rayner, J. T. 2003, PASP, 115, 389
Valenti, J. A., Marcy, G. W., & Basri, G. 1995, ApJ, 439, 939
West, A. A., & Basri, G. 2009, ApJ, 693, 1283
Wilson, O. C. 1966, ApJ, 144, 695
Winters, J. G., Henry, T. J., Jao, W.-C., et al. 2019, AJ, 157, 216
Yuk, I.-S., Jaffe, D. T., Barnes, S., et al. 2010, Proc. SPIE, 7735, 77351M
Zeeman, P. 1897, ApJ, 5, 332